Geophysical Journal International

Geophys. J. Int. (2016) **204,** 74–93 doi: 10.1093/gji/ggv410

GJI Geomagnetism, rock magnetism and palaeomagnetism

3-D magnetotelluric inversion including topography using deformed hexahedral edge finite elements and direct solvers parallelized on SMP computers – Part I: forward problem and parameter Jacobians

M. Kordy,[1,2] P. Wannamaker,[2] V. Maris,[2] E. Cherkaev[1] and G. Hill[3]

[1]*Department of Mathematics at the University of Utah,* 155 *S* 1400 *E Room* 233, *Salt Lake City, UT* 84112-0090, *USA. E-mail: kordy@math.utah.edu*

[2]*Energy and Geoscience Institute at the University of Utah,* 423 *Wakara Way, Suite* 300, *Salt Lake City, UT* 84108, *USA*

[3]*Gateway Antarctica, University of Canterbury, Private Bag* 4800 *Christchurch* 8140 *and Antarctica Scientific Limited, Unit* 5*E*/39 *Taranaki Street Wellington* 6011

Accepted 2015 September 23. Received 2015 September 22; in original form 2014 November 3

SUMMARY

We have developed an algorithm, which we call HexMT, for 3-D simulation and inversion of magnetotelluric (MT) responses using deformable hexahedral finite elements that permit incorporation of topography. Direct solvers parallelized on symmetric multiprocessor (SMP), single-chassis workstations with large RAM are used throughout, including the forward solution, parameter Jacobians and model parameter update. In Part I, the forward simulator and Jacobian calculations are presented. We use first-order edge elements to represent the secondary electric field (E), yielding accuracy $O(h)$ for E and its curl (magnetic field). For very low frequencies or small material admittivities, the E-field requires divergence correction. With the help of Hodge decomposition, the correction may be applied in one step after the forward solution is calculated. This allows accurate E-field solutions in dielectric air. The system matrix factorization and source vector solutions are computed using the MKL PARDISO library, which shows good scalability through 24 processor cores. The factorized matrix is used to calculate the forward response as well as the Jacobians of electromagnetic (EM) field and MT responses using the reciprocity theorem. Comparison with other codes demonstrates accuracy of our forward calculations. We consider a popular conductive/resistive double brick structure, several synthetic topographic models and the natural topography of Mount Erebus in Antarctica. In particular, the ability of finite elements to represent smooth topographic slopes permits accurate simulation of refraction of EM waves normal to the slopes at high frequencies. Run-time tests of the parallelized algorithm indicate that for meshes as large as $176 \times 176 \times 70$ elements, MT forward responses and Jacobians can be calculated in $\sim$1.5 hr per frequency. Together with an efficient inversion parameter step described in Part II, MT inversion problems of 200–300 stations are computable with total run times of several days on such workstations.

Key words: Numerical approximations and analysis; Electrical properties; Magnetotelluric; Geomagnetic induction; Physics of magma and magma bodies; Antarctica.

1 INTRODUCTION

Impressive progress has been made over the past several years in the simulation and inversion of three-dimensional (3-D) diffusive electromagnetic (EM) responses for earth electrical resistivity structure. Most approaches have adopted finite difference or finite element (FE) numerical methods although the integral equations technique also has been utilized (see reviews by Börner 2010; Everett 2012). An effective simulation and inversion algorithm needs to handle a large range of structural scales due to possibly complex resistivity distributions and the wide frequency bandwidth of survey techniques (e.g. potentially seven or more orders of magnitude in magnetotellurics (MTs); Chave & Jones 2012). Furthermore, in many orogenic or resource settings, the earth's surface can show considerable topographic variation which will have its own EM response and introduces vertical variation of receiver placement with respect to subsurface structure.

To include topography in earth resistivity models, we pursue the FE method. FEs allow for a relatively smooth representation of topography. Although it is possible to consider finite difference or finite volume discretization on unstructured (i.e. non stair-stepped) meshes (Hyman & Shashkov 1999; Liu *et al.* 2009; Jahandari & Farquharson 2014), it may lead to spurious modes in the solution (see a discussion in Hyman & Shashkov 1999), late time instability

(see a discussion in Liu *et al.* 2009) or geometric restrictions on the grid (Liu *et al.* 2009). Proper discretization of the operators ∇, $\nabla \times$ and $\nabla \cdot$ that are important in Maxwell's equations (Hyman & Shashkov 1999) is a challenge for unstructured meshes. Edge elements, considered in this paper, respect the relationship between those operators, expressed by an algebraic topology structure called de Rham diagram (Gunzburger & Bochev 2009), which allows us to apply the divergence correction in a natural way.

Several authors have considered the choice between tetrahedral and hexahedral elements for including topography (e.g. daSilva *et al.* 2012; Lelièvre & Farquharson 2013; Schwarzbach & Haber 2013), with tetrahedra argued by some to allow a more arbitrary discretization of structure. However, we will show that much can be accomplished using hexahedra, and their simpler implementation in both the forward and inverse modules helps to keep computer resources manageable and may facilitate wider transfer of technique within the EM community. We solve for the electric field through the governing Helmholtz equation, so edge FEs are used (lowest order type) (Nédélec 1986). These conforming elements allow field discontinuities normal to conductivity interfaces to be represented but preserve continuity of the tangential field component. FEs do not invoke material averaging procedures across cell boundaries as is done in staggered grid finite difference schemes (daSilva *et al.* 2012) so there is no question about the placement of sharp interfaces.

The design factors cited above can put high demands upon mesh discretization and computing resources for larger data sets. Because of such demands, especially memory, iterative solutions have dominated the literature heretofore (Haber *et al.* 2007; Börner *et al.* 2008; Commer & Newman 2008; Um *et al.* 2012, and many others). Since at least the work of Pridmore *et al.* (1981), however, iterative forward solvers are known to become ill-conditioned and slow to converge if grid cell aspect ratios grow to be extreme. Moreover, iterative solutions for the Helmholtz equation require careful preconditioning and even so may sometimes fail to converge (also see Grayver *et al.* 2013). They become expensive when many right-hand source vectors are needed, such as in controlled-source applications or the inversion approach we describe, as each source requires the work of a full simulation. Conditioning issues may apply as well to iteratively solving normal equations in the inversion parameter step (*op. cit.*).

Recent advances in computing power, especially emergence of less expensive many-core, symmetric multiprocessor (SMP) workstations with substantial RAM, have motivated us to implement direct solvers both for the forward model responses and for Gauss–Newton inversion parameter steps. This is intended to produce a practical 3-D inversion code incorporating topography that can handle moderately large data sets on an affordable, single-box computer format. We find that accurate solutions for meshes with large element aspect ratios having run times nearly independent of frequency are possible. The solution of hundreds of source vectors at the cost of factoring the forward system matrix allows explicit calculation of parameter Jacobians accurately and efficiently, as has been applied for some time with the 2-D problem (e.g. deGroot-Hedlin & Constable 1990; deLugao & Wannamaker 1996; Key & Constable 2011).

We certainly are not the first to examine direct solutions for 3-D problems. Streich (2009) created a staggered-grid finite difference algorithm with a direct solver for simulating marine controlled source electromagnetic (CSEM) responses. Oldenburg *et al.* (2008, 2013) used a direct solver in their finite difference H-field simulator for time domain electromagnetic (TDEM) inversion and Um *et al.* (2015) used a mixed direct-iterative solution to model well casing effects with FEs. daSilva *et al.* (2012) utilized rectilinear edge FEs in forward modelling of seafloor CSEM models while Ren *et al.* (2013) considered a direct solver for tetrahedral meshes. Grayver *et al.* (2013) incorporated Streich's solver to compute forward responses and parameter Jacobians explicitly and create an inversion algorithm where the parameter step was estimated using a pre-conditioned conjugate gradient (PCG) scheme. Schwarzbach & Haber (2013) developed an unstructured mesh of tetrahedra with the forward problem solved directly and the parameter step computed via PCG or iterative quasi-Newton method. Usui (2015) solved MT responses directly using a tetrahedral mesh and developed an inversion code with direct solution of the parameter step in model space.

In Part I of our contribution, we apply a direct solver to edge FE equations of a deformed hexahedral mesh and verify that accurate responses are achieved for subsurface and topographic structure. Good responses are obtained also in the dielectric air portion of the model after applying a divergence correction. Parameter Jacobians are computed accurately and efficiently in the direct framework exploiting reciprocity. Moderately large meshes can be computed in what we believe are practical run times. In Part II, forward simulations are used together with MT data to form normal equations for a regularized inversion step. We investigate the data space (Siripunvaraporn *et al.* 2005) formulations of the step and confirm that it can handle significant parameter sets. We invert a well-known field data set to demonstrate algorithm performance in real-world settings. The HexMT algorithm, is parallelized for widely available, server-class SMP workstations.

2 FINITE ELEMENT FORMULATION

For representing structure with topography, we use an FE mesh such as in Fig. 1. Corners of elements at the air-earth interface (surface) are adjusted vertically to represent elevation changes. This is similar to the fashion of Nam *et al.* (2007). Sub- and superajacent element layers are moved similarly but with steadily diminishing magnitude away from the surface until upper and lower datum planes are reached. Beyond those planes, the element layers remain flat. The height and depth of these planes from the background air-earth interface typically is several times the maximal topographic model relief to allow the elements to be close to parallelepipeds in shape. If there are elements that are not close to parallelepipeds, the order of convergence versus discretization may be reduced (see Falk *et al.* 2011).

Formally, the spatial domain of Fig. 1 is a cuboid Ω, whose top portion is air ($\sigma = 0$) and whose lower portion is earth's subsurface ($\sigma > 0$) which may exhibit topography in its central portion. We assume that the conductivity of the earth's subsurface may be an arbitrary 3-D isotropic function in the middle of the domain, while towards the distant domain boundaries the conductivity becomes 1-D with flat topography, that is, changing only vertically. In the frequency domain with $e^{i\omega t}$ time dependence, where ω is the angular frequency, the physical property variables are admittivity $\hat{\sigma} = \sigma + i\omega\epsilon$ with electrical conductivity $\sigma \geq 0$, dielectric permittivity $\epsilon > 0$, and magnetic permeability $\mu > 0$.

Similar to numerous other authors (e.g. following Hohmann 1988), we define (E^p, H^p) as primary fields, which would be those within and over the 1-D host, for use as an impressed source J^{imp}. Thus we denote

$$J^{\text{imp}} = -(\hat{\sigma} - \hat{\sigma}^p)E^p \tag{1}$$

Secondary and primary fields are added to obtain total fields as:

$$E^t = E + E^p, \quad H^t = H + H^p \tag{2}$$

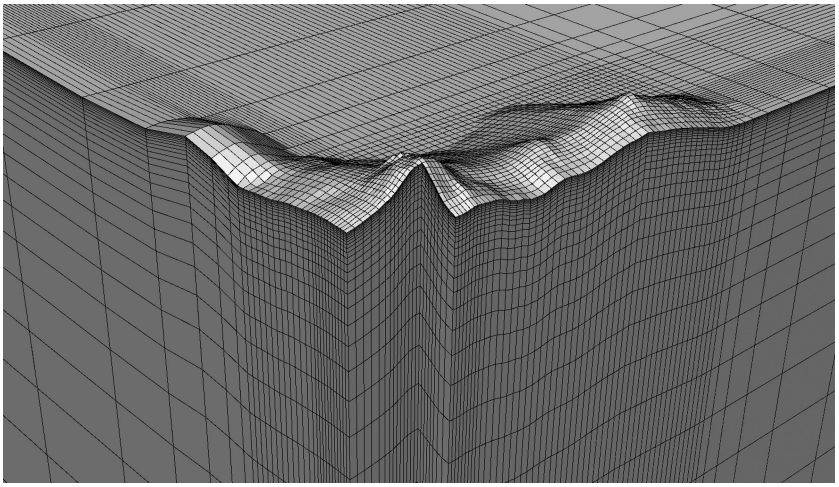

Figure 1. 3-D view of an example hexahedral mesh with topography. Only the underground part of the mesh is shown. One sees increasingly high aspect ratio of elements approaching the boundary $\partial\Omega$. This view is from the southwest of mesh number 3 for Mount Erebus model analysed later.

One assumes that far from conductivity inhomogeneity, that is, near $\partial\Omega$,

$$E^t \approx E^p, \quad H^t \approx H^p \tag{3}$$

and thus the secondary electric field satisfies $E \approx 0$ near the domain boundary.

The secondary field E obeys the vector Helmholtz equation in the open spatial domain $\Omega \subset \mathbb{R}^3$:

$$\nabla \times \left(\frac{1}{\mu}\nabla \times E\right) + \mathrm{i}\omega\hat{\sigma}E = -\mathrm{i}\omega(\hat{\sigma} - \hat{\sigma}^p)E^p \tag{4}$$

(Hohmann 1988). As a basis for FE formulation, we will consider a weak form of eq. (4) (*cf.* Monk 1992):

$$\int_\Omega \frac{1}{\mu}\nabla \times E \cdot \nabla \times M + \mathrm{i}\omega \int_\Omega \hat{\sigma}E \cdot M = \mathrm{i}\omega \int_\Omega J^{\mathrm{imp}} \cdot M \tag{5}$$

satisfied for all $M \in \mathcal{H}_0(\nabla\times, \Omega)$. The solution E should be a member of the same Sobolev space $\mathcal{H}_0(\nabla\times, \Omega)$ which is formally defined as

$$\mathcal{H}_0(\nabla\times, \Omega) = \left\{ M{:}\Omega \to \mathbb{C}^3 : \int_\Omega \left(|M|^2 + |\nabla \times M|^2\right) < \infty, \right.$$
$$\left. n \times M|_{\partial\Omega} = 0 \right\} \tag{6}$$

It is a space of complex valued vector fields that are square integrable with square integrable curl. Heuristically, one can think of the members of this space as having continuous tangential components across any surface going through Ω. $\mathcal{H}_0(\nabla\times, \Omega)$ is a natural space for the electric field E. The boundary condition $n \times E = 0$ is a natural consequence of eqs (2) and (3).

For numerical approximation, we choose first-order edge elements $\mathcal{H}_0^h(\nabla\times, \Omega)$ on a hexahedral mesh (see Nédélec 1986). By construction $\mathcal{H}_0^h(\nabla\times, \Omega) \subset \mathcal{H}_0(\nabla\times, \Omega)$ and as the mesh element size $h \to 0$, $\mathcal{H}_0^h(\nabla\times, \Omega)$ approaches $\mathcal{H}_0(\nabla\times, \Omega)$. The tangential components of the members of $\mathcal{H}_0^h(\nabla\times, \Omega)$ are continuous across elements while the normal component may experience a jump. Degrees of freedom of the first-order edge elements are related to the integral of the E-field along an edge. Through Stokes' theorem, an integration of E along the edges, around the face yields the flux of $\nabla \times E$ through the face. This shows that edge element discretization is compatible with the curl operator.

The electric field over Ω is represented as a linear combination of the edge shape functions N_i with coefficients ξ_i:

$$E = \sum_{i=1}^{n_e} \xi_i N_i \tag{7}$$

where $i = 1, \ldots, n_e$ are indices of the edges that do not lie on the boundary. By excluding the edges lying on the boundary one imposes the boundary condition of $n \times E = 0$ on $\partial\Omega$. It is equivalent to setting the coefficients related to the edges lying on the boundary to zero. By substituting eq. (7) into eq. (5) and using N_j as test functions, one obtains a linear system (*cf.* Monk 1992)

$$A\xi = b \tag{8}$$

$$A_{i,j} = \left[\int_\Omega \frac{1}{\mu}\nabla \times N_i \cdot \nabla \times N_j + \mathrm{i}\omega \int_\Omega \hat{\sigma}N_i \cdot N_j\right] \tag{9}$$

$$b_i = \mathrm{i}\omega \int_\Omega J^{\mathrm{imp}} \cdot N_i. \tag{10}$$

The secondary magnetic field is calculated as

$$H = \frac{-\nabla \times E}{i\omega\mu}. \tag{11}$$

This justifies the choice of first-order edge elements which have the same accuracy $O(h)$ for both the field and the curl.

Note that 1-D host layer interfaces may project through individual deformed elements and as a result J^{imp} is discontinuous within an element. The integration of terms in eqs (9) and (10) is done using a quadrature integration of the form

$$\sum_{i=1}^{n} f(u_i)v_i, \tag{12}$$

where u_i are points in the reference element, which is a unit cube in our case and v_i are weights. If the integrand f is smooth in the element, which is true for eq. (9) and for eq. (10) if the 1-D host layer interface does not project through an element, positions u_i and weights v_i are set according to Gaussian quadrature. Yet for eq. (10), if a 1-D conductivity layer interface splits the element, the integrated function is discontinuous and the integration is done by distributing u_i uniformly in the unit cube and setting all $v_i = \frac{1}{n}$. For accuracy of integration, n should have larger values than in the case of a smooth function. As will be seen, with sufficiently fine integration of the

primary field over the element conductivity differences, we are able to achieve accurate responses. For the numerical integration, we use 10 points in each direction, which results in 1000 points in each element. To limit the additional computational effort due to the evaluation of the source term at so many points, such an integration is done only if the layer boundary crosses the element.

In this paper we consider the MT source, namely that of a vertically propagating, planar EM wave. The total field components at specified surface locations and frequencies are interrelated through the tensor impedance Z and tipper K as

$$\begin{bmatrix} E_x^t \\ E_y^t \\ H_z^t \end{bmatrix} = \begin{bmatrix} Z_{xx} & Z_{xy} \\ Z_{yz} & Z_{yy} \\ K_{zx} & K_{zy} \end{bmatrix} \begin{bmatrix} H_x^t \\ H_y^t \end{bmatrix}, \tag{13}$$

where subscripts x, y, z denote components of a vector field. Eq. (8) is solved twice for two polarizations ($k = 1, 2$) of the source field E^p, typically in the x- and then the y-directions, to generate two equations in two unknowns for each row of the tensor (13). The equations expressing the impedance in terms of the electric and magnetic fields are listed in, for example, Newman & Alumbaugh (2000) and can be written analogously for the tipper.

A receiver can be positioned at an arbitrary location $\mathbf{r}$ with respect to element edges via appropriate interpolation. In general, let $\mathbf{r}$ be inside an element with edges $e_1, \ldots, e_{12}$. Then field E^k at location $\mathbf{r}$ is given by

$$E^k(\mathbf{r}) = \sum_{l=1}^{12} N_{e_l}(\mathbf{r})\xi_{e_l} = \begin{bmatrix} (w_x^E)^T \xi^k \\ (w_y^E)^T \xi^k \\ (w_z^E)^T \xi^k \end{bmatrix}. \tag{14}$$

Here w_x^E, w_y^E, w_z^E contain interpolation vectors with at most 12 non-zero values corresponding to x, y and z components of edge shape functions $N_{e_1}(\mathbf{r}), \ldots, N_{e_{12}}(\mathbf{r})$.

Similarly, the secondary magnetic field $H^k(\mathbf{r})$ for polarization k, calculated using eq. (11) at location $\mathbf{r}$, is given by

$$H^k(\mathbf{r}) = \sum_{l=1}^{12} \frac{\nabla \times N_{e_l}(\mathbf{r})}{-i\omega\mu}\xi_{e_l} = \begin{bmatrix} (w_x^H)^T \xi^k \\ (w_y^H)^T \xi^k \\ (w_z^H)^T \xi^k \end{bmatrix}. \tag{15}$$

This time the only non-zero values of w_x^H, w_y^H, w_z^H are x, y and z components of

$$\left(\frac{\nabla \times N_{e_1}(\mathbf{r})}{-i\omega\mu}, \ldots, \frac{\nabla \times N_{e_{12}}(\mathbf{r})}{-i\omega\mu} \right).$$

Total fields are obtained as in eq. (2).

The locations of the MT receivers are on the Earth's surface, which is always at an element's face. The along-face (tangential) components of the discretized electric field experience a jump at the face edges, thus it is best to use the values of the field calculated at the face centre. One could evaluate the field elsewhere by interpolation of the fields from the neighbouring face centres, yet for simplicity we assume that the receiver's location $\mathbf{r}$ is at the face centre. This requires MT receiver relocations in practice. In our inversions (see our companion paper, Kordy *et al.* 2015b) we consider the element size to be several times smaller than the distance between the receivers, thus the relocation is not very large and does not appear to lead to a significant inversion error (see subsequent Mount Erebus simulation and the brick-under-hill synthetic inversion of Kordy *et al.* 2015b).

Because the tangential electric field is continuous across the surface, it is immaterial whether we approach the surface from within an element below or above the air-earth interface. E-fields normal to a surface are discontinuous and must be evaluated on the side of interest, or interpolated using the values of the total electric current at the element centres. If magnetic permeability μ is the same above and below the surface, the magnetic field should be continuous as well. However, because the H-field obtained through curl E is piecewise constant from element face to face, we use an average of the H-field from the elements on either side of a receiver. As a result interpolation vectors w corresponding to the magnetic field may have up to 20 non-zero entries. The interpolation vectors w depend neither on the primary source fields nor on the conductivity model σ.

To calculate the MT response apart from solving eq. (8) one needs to evaluate the entries of matrix A as well as calculate the source vectors b (eq. 10). In our implementation using OpenMP, for a model with a mesh with 101, 101 and 50 cells in the x, y and z directions, respectively ($101x\,101y\,50z$) and 256 MT receivers, the calculation of the system matrix takes about 1.7 per cent of the time of the forward modelling (response F and Jacobian J). We have parallelized the calculation of the source vectors (10) also using OpenMP. If 9-point quadrature is used for all elements, the time of the calculation of the right hand side (rhs) vectors, for the same model, is about 0.15 per cent of the total forward modelling time. In practice, if the background conductivity layer crosses an element, we use a quadrature with 1000 points, which increases the computational time. Yet even if the quadrature with 1000 points is used for all of the elements, the time of computation is around 0.8 per cent of the total forward modelling time.

3 DIVERGENCE CORRECTION

Smith (1996) recognized that matrices formed from the numerical approximation of eq. (4) suffer from a particular ill-conditioning. This is why researchers considered solving for vector and scalar potentials (Haber *et al.* 2000; Mitsuhata & Uchida 2004; Roy 2007; Kordy *et al.* 2015a). The second term on the left side of eq. (4) becomes very small at either low frequencies or small admittivities, so the solution becomes vulnerable to parasitic curl-free fields. These are manifest as erroneous divergences of current density within the earth model that require corrective steps. For example, consider linear system (8) whose true solution is ξ, approximated by eq. (7). Let the gradient of a potential field be added to the solution such that

$$\hat{E} = E + \nabla\tilde{\varphi} = \sum_{i=1}^{n_e} \hat{\xi} N_i \tag{16}$$

and let the values of $\nabla\tilde{\varphi}$ be of order 1. The residual r of eq. (7) is defined by:

$$r = A\hat{\xi} - b = A\xi - b + A(\hat{\xi} - \xi) = A(\hat{\xi} - \xi). \tag{17}$$

The ith component of the residual vector r is

$$r_i = \sum_{j=1}^{n_e} A_{i,j}(\hat{\xi_j} - \xi_j),$$

which for the air ($\hat{\sigma} = i\omega\epsilon_0$) reduces to

$$r_i = -\omega^2\epsilon_0 \int_\Omega N_i \cdot \nabla\tilde{\varphi}.$$

Thus, the residual will be nonzero, but very small—of the order $\omega^2\epsilon_0$ for air. Even if we modify the field substantially by adding

$\nabla\tilde{\varphi}$, there may be hardly any difference in the residual value. An eigenvalue analysis of ill-conditioning of eq. (8) is presented in Appendix A.

For iterative solutions to eq. (8), the typical procedure for removing spurious curl-free fields, called divergence correction, is to compute several solution iterations, estimate current divergences over the discretized model domain, calculate the curl-free fields arising from such divergences and remove these fields from the full iterative solution at that stage (e.g. Smith 1996; Newman & Alumbaugh 2000; Sasaki 2001; Siripunvaraporn *et al.* 2002; Farquharson & Miensopust 2011). This is repeated numerous times until final convergence. One can also add the divergence condition to the system of equations (Vardapetyan & Demkowicz 1999; Schwarzbach 2009; Grayver *et al.* 2013) although that increases the number of unknowns in the linear system. For example, Grayver *et al.* (2013) in their approach increase the number of unknowns by one-third.

We present an alternative technique that achieves an efficient and accurate divergence correction for our FE method. Consider any domain Ω, with spatially changing conductivity $\hat{\sigma}$, which includes both air and the subsurface. The space $\mathcal{H}_0(\nabla\times,\Omega)$, defined in eq. (6), may be decomposed into the null space of the curl and the space orthogonal to it (Gunzburger & Bochev 2009). Specifically:

$$\mathcal{H}_0(\nabla\times,\Omega) = R(\nabla)\oplus R(\nabla)^{\perp_{\hat{\sigma}}} \tag{18}$$

For every $M\in\mathcal{H}_0(\nabla\times,\Omega)$, there is a unique decomposition:

$$M=\nabla\varphi_M + M_\perp,\quad \varphi_M\in H_0^1(\Omega),\ \ M_\perp\in R(\nabla)^{\perp_{\hat{\sigma}}} \tag{19}$$

where

$$\begin{aligned}
\mathcal{H}_0^1(\Omega) &= \left\{\varphi:\Omega\to\mathbb{C} \quad : \int_\Omega \left(|\varphi|^2+|\nabla\varphi|^2\right)<\infty,\ \varphi|_{\partial\Omega}=0\right\}\\
R(\nabla) &= \{\nabla\varphi \quad : \varphi\in\mathcal{H}_0^1(\Omega)\}\\
R(\nabla)^{\perp_{\hat{\sigma}}} &= \left\{M\in\mathcal{H}_0(\nabla\times,\Omega) \quad : \int_\Omega \hat{\sigma}M\cdot\nabla\varphi=0\ \ \forall\varphi\in\mathcal{H}_0^1(\Omega)\right\}
\end{aligned}$$

Space $\mathcal{H}_0^1(\Omega)$ is a space of complex valued scalar potentials, the square integrable scalar fields which have a gradient that is square integrable. One can think of the members of this space as of scalar functions that are continuous across any surface inside the domain. The '0' subscript corresponds to the assumption of zero value on the boundary Ω. Once the gradient ∇ is applied to those functions one obtains the space $R(\nabla)$. Because $\nabla\times\nabla\varphi=0$, $R(\nabla)$ is in the null space of the curl. Moreover, the range of the gradient on $\mathcal{H}_0^1$ is exactly equal to the null space of the curl in the space $\mathcal{H}_0(\nabla\times,\Omega)$ (Gunzburger & Bochev 2009). For more thorough discussion of Sobolev spaces $\mathcal{H}_0(\nabla\times,\Omega)$ and $\mathcal{H}_0^1(\Omega)$ see Girault & Raviart (1986) and Adams & Fournier (2003). The decomposition in eq. (18) allows us to represent a field from $\mathcal{H}_0(\nabla\times,\Omega)$ as a sum of two fields, one in the null space and the other orthogonal to it. This decomposition is called the Helmholtz decomposition or the Hodge decomposition of $\mathcal{H}_0(\nabla\times,\Omega)$. The proof of its existence for the case of a constant $\hat{\sigma}$ may be found in Amrouche *et al.* (1998). For a proof given our case of non-constant $\hat{\sigma}$ when Ω includes both air and the earth's subsurface, one should consider a Poisson equation for φ_M:

$$\int_\Omega \hat{\sigma}\nabla\varphi_M\cdot\nabla\phi = \int_\Omega \hat{\sigma}M\cdot\nabla\phi$$

for $\varphi_M,\ \phi\in\mathcal{H}_0^1$, which has a unique solution.

In the case of a constant $\hat{\sigma}$, it is a decomposition into a curl-free part $\nabla\varphi_M$ and a divergence-free part $M_\perp$, which is orthogonal to $R(\nabla)$. In the constant $\hat{\sigma}$ case it is the same as representing the original field using a vector and a scalar potential with a Coulomb gauge, in which case the vector potential is divergence free (Mitsuhata & Uchida 2004).

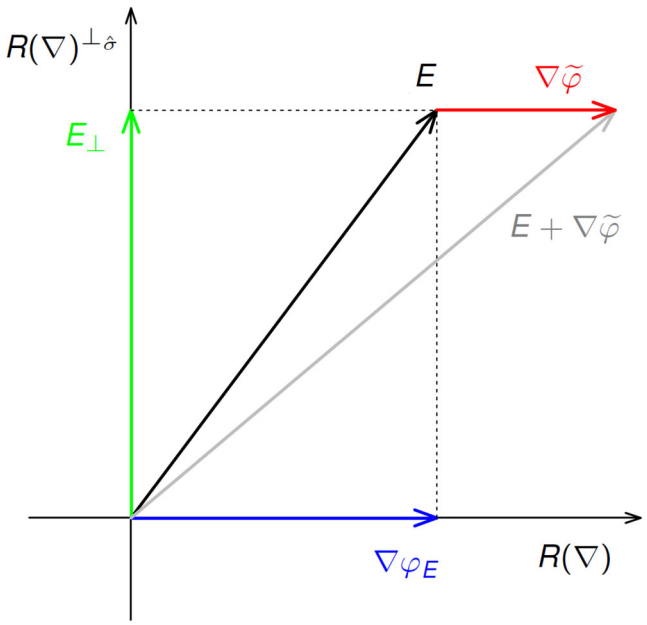

Figure 2. Hodge decomposition of the solution E, together with the added error of the form $\nabla\tilde{\varphi}$.

In our context, when $\hat{\sigma}\neq$ constant, we have $\nabla\cdot(\hat{\sigma}M_\perp)=0$, which may be seen through integration by parts of the condition defining $R(\nabla)^{\perp_{\hat{\sigma}}}$. Also, if $\hat{\sigma}\in\mathbb{R}$ and $\hat{\sigma}>0$ one may interpret the space $R(\nabla)^{\perp_{\hat{\sigma}}}$ as the space orthogonal to $R(\nabla)$ with an inner product having $\hat{\sigma}$ as the weight.

To visualize the subsequent derivations consider Fig. 2. Let the solution E to eq. (5) be represented using the Hodge decomposition (19), namely

$$E=\nabla\varphi_E+E_\perp,\quad \varphi_E\in H_0^1(\Omega),\ \ E_\perp\in R(\nabla)^{\perp_{\hat{\sigma}}}. \tag{20}$$

By setting $M=M_\perp\in R(\nabla)^{\perp_{\hat{\sigma}}}$ and then $M=\nabla\varphi$, one can show that eq. (5) is equivalent to two uncoupled equations on $R(\nabla)^{\perp_{\hat{\sigma}}}$ and $R(\nabla)$ respectively:

$$\begin{aligned}
\int_\Omega \frac{1}{\mu}\nabla\times E_\perp\cdot\nabla\times M_\perp + \mathrm{i}\omega\int_\Omega \hat{\sigma}E_\perp\cdot M_\perp &= \mathrm{i}\omega\int_\Omega J^{\mathrm{imp}}\cdot M_\perp\\
\mathrm{i}\omega\int_\Omega \hat{\sigma}\nabla\varphi_E\cdot\nabla\varphi &= \mathrm{i}\omega\int_\Omega J^{\mathrm{imp}}\cdot\nabla\varphi.
\end{aligned} \tag{21}$$

The first equation is satisfied $\forall M_\perp\in R(\nabla)^{\perp_{\hat{\sigma}}}$, the second $\forall\varphi\in\mathcal{H}_0^1(\Omega)$. The second equation ensures that the component $\nabla\varphi_E$ is proper, so if we impose this equation, we may remove the error of the form $\nabla\tilde{\varphi}$. In a discrete case, we are dealing with $\mathcal{H}_0^h(\nabla\times,\Omega)$, which is the space of first-order edge elements. An important property of this space is that a Hodge decomposition similar to eq. (18) exists (see Gunzburger & Bochev 2009). The space $\mathcal{H}_0^1(\Omega)$ has to be replaced with $\mathcal{H}_0^{1,h}(\Omega)$—the space spanned by first-order nodal shape functions on the same mesh.

The correction is applied as follows. Let E, be an approximation of the electric field given by eq. (7). Solve Poisson equation for $\nabla\varphi_{\mathrm{corr}}\in\mathcal{H}_0^{1,h}(\Omega)$, $\forall\varphi\in\mathcal{H}_0^{1,h}(\Omega)$:

$$\mathrm{i}\omega\int_\Omega \hat{\sigma}\nabla\varphi_{\mathrm{corr}}\cdot\nabla\varphi = \mathrm{i}\omega\int_\Omega (\hat{\sigma}E-J^{\mathrm{imp}})\cdot\nabla\varphi. \tag{22}$$

The corrected electric field $E_{\rm corr}$ is

$$E_{\rm corr} = E - \nabla\varphi_{\rm corr}. \tag{23}$$

Note that the corrected field satisfies the original eq. (5) in a discrete setting for $E, M \in \mathcal{H}_0^h(\nabla\times, \Omega)$. In fact, if infinite precision was used to solve eq. (5) numerically, there would be no need for the correction. The correction considers the original equation on a subspace and removes a numerical error introduced by a direct solver that uses finite precision.

The correction may be given further justification by considering the second equation in eq. (21). Using the fact that $E_\perp = E - \nabla\varphi_E \in R(\nabla)^{\perp_{\hat\sigma}}$ and integrating by parts, we obtain:

$$\mathrm{i}\omega \int_\Omega (\nabla\cdot(\hat\sigma E))\varphi = \mathrm{i}\omega \int_\Omega (\nabla\cdot J^{\rm imp})\varphi. \tag{24}$$

Thus, we ensure that the divergence of electric current is proper weakly, on average, with $\varphi \in \mathcal{H}_0^{1,h}(\Omega)$ as a weight. The right-hand side of eq. (22) may be viewed as excessive divergence of the electric current, which is removed when eq. (23) is applied.

Divergence correction requires solving the Poisson eq. (22), which we do using nodal-based FEs. The divergence correction system matrix has three times less variables than the original system matrix, and at least four times less non-zeroes. In our experience, the divergence correction requires much less run time than solving the original system (8); factorization phase is at least eight times faster and solve phase is at least five times faster.

Although the main computational cost is related to the solution of the linear system (22), it is not the only cost of the divergence correction. One needs to calculate the system matrix of eq. (22), evaluate the right-hand side of eq. (22), and once $\varphi_{\rm corr}$ is obtained one needs to apply the correction using eq. (23). We have parallelized those calculations using MKL SparseBLAS library as well as using OpenMP. After parallelization, all of those additional calculations for a model with a mesh $101x\ 101y\ 50z$ and 256 MT receivers are more than 2.5 times faster than the solution of eq. (22) using MKL PARDISO and constitute about 3.4 per cent of the forward modelling time. The divergence correction sparse solve with MKL PARDISO takes about 9 per cent of the forward modelling time.

4 FIELD AND MT RESPONSE JACOBIANS

A primary goal in developing the FE simulator is to apply it to non-linear inversion of MT field data. As described more fully in our companion paper, we examine both model and data space approaches to parameter updates under the Gauss–Newton framework (Siripunvaraporn *et al.* 2005). For defining terms as related to FE simulation, the model space update equation is (e.g. Tarantola 2005; Mackie *et al.* 1988):

$$\begin{aligned}&[J^T B_d J + \lambda B_m](m_{n+1} - m_0)\\ &\quad = J^T B_d[d - F(m_n) + J(m_n - m_0)],\end{aligned} \tag{25}$$

where $F(m_n)$ is the MT response at iteration n using our FE code, d is the vector of N_d observed MT data weighted against their estimated covariance matrix B_d^{-1}, B_m^{-1} is a model covariance matrix which stabilizes or regularizes the N_m model parameter variations, m_0 is a reference model, and λ is a constant controlling trade-off between data fit and model parameter stabilization.

Term J is the N_d by N_m matrix of parameter Jacobians or derivatives (Tarantola 2005) which specify the incremental change in the value of an MT response datum (in Z or K) to an incremental change in the value of a subsurface electrical conductivity parameter. First, we focus on the derivatives of the secondary fields. There have been numerous ways to express this in the literature (e.g. McGillivray *et al.* 1994); here we basically generalize from the 2-D approach of deLugao & Wannamaker (1996). Recalling the interpolation vectors w, consider an entry σ_j of the FE mesh conductivity vector σ. The entry may correspond to a single element or a group of them. The derivative of a field value $w^T\xi^k$ with respect to σ_j may be evaluated as:

$$\begin{aligned}\frac{\partial(w^T\xi^k)}{\partial\sigma_j} &= w^T\frac{\partial\xi^k}{\partial\sigma_j} = w^T\frac{\partial(A^{-1}b^k)}{\partial\sigma_j} = w^T\left[\frac{\partial A^{-1}}{\partial\sigma_j}b^k + A^{-1}\frac{\partial b^k}{\partial\sigma_j}\right]\\ &= w^T\left[\left(-A^{-1}\frac{\partial A}{\partial\sigma_j}A^{-1}\right)b^k + A^{-1}\frac{\partial b^k}{\partial\sigma_j}\right]\\ &= w^T\left[-A^{-1}\frac{\partial A}{\partial\sigma_j}(A^{-1}b^k) + A^{-1}\frac{\partial b^k}{\partial\sigma_j}\right]\\ &= w^T\left[-A^{-1}\frac{\partial A}{\partial\sigma_j}\xi^k + A^{-1}\frac{\partial b^k}{\partial\sigma_j}\right]\end{aligned}$$

for source polarization k. This reduces to

$$\frac{\partial(w^T\xi^k)}{\partial\sigma_j} = w^T\left(A^{-1}\left[-\frac{\partial A}{\partial\sigma_j}\xi^k + \frac{\partial b^k}{\partial\sigma_j}\right]\right). \tag{26}$$

As written, in order to calculate the derivatives of the field values with respect to all $(\sigma_j)_{j=1}^{N_m}$, one would have to solve one linear equation for each polarization and for each σ_j, and then multiply by the proper w, to obtain the desired derivatives. That yields $2\cdot N_m$ linear systems to solve, where N_m is the number of inversion cells. However, exploiting interchangeability of sources and receivers in reciprocity, or using the adjoint method, or simply using the associativity of the matrix multiplication, eq. (26) may be rewritten as

$$\begin{aligned}\frac{\partial(w^T\xi^k)}{\partial\sigma_j} &= \left(w^TA^{-1}\right)\left[-\frac{\partial A}{\partial\sigma_j}\xi^k + \frac{\partial b^k}{\partial\sigma_j}\right]\\ &= \left(A^{-T}w\right)^T\left[-\frac{\partial A}{\partial\sigma_j}\xi^k + \frac{\partial b^k}{\partial\sigma_j}\right].\end{aligned} \tag{27}$$

In this form we solve one linear system for each field component. The method yields $5\cdot N_{\rm rec}$ linear systems to solve, where $N_{\rm rec}$ denotes the number of receivers. The matrix A, defined at (9), is symmetric, so $A^{-T} = A^{-1}$. To calculate $A^{-1}w$, we are solving a linear system where the source w, defined in eqs (14) and (15), is distributed on the edges surrounding the receiver location (*cf.* deLugao & Wannamaker 1996).

Jacobians for impedance Z and tipper K at each receiver follow by applying the chain rule to the equations for the impedance and tipper elements of eq. (13) defined from applying the two source polarizations $k = 1, 2$. The individual impedance element derivatives are listed in Newman & Alumbaugh (2000) and the tipper element derivatives follow by analogy. For inversion implementation, derivatives are converted to be with respect to $\log_{10}$ resistivity (Hohmann & Raiche 1988).

The main computational cost of the calculation of the Jacobian is the factorization of A and application of its inverse to w, for which example run times are given further in the paper. Yet one also needs to use the result of this calculation in eq. (27). And as for large models the Jacobian matrix is large, it might take a notable time to fill its entries in the memory. In our implementation with OpenMP the time of evaluation of eq. (27), once $(A^{-T}w)$ is obtained, and the successive evaluation of the derivative of Z and K with respect to

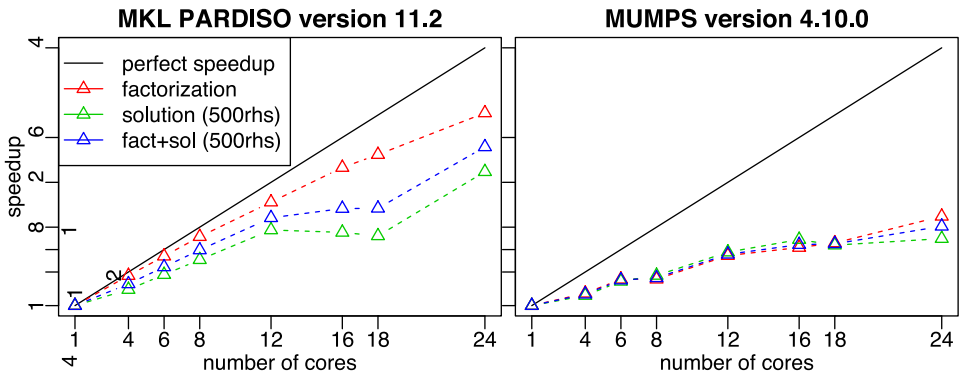

Figure 3. Speedup of MKL PARDISO and MUMPS for a fixed problem with mesh with 85x 85y 50z cells on a single workstation with 24 cores. For PARDISO, runs with different number of OpenMP threads are compared. For MUMPS, we present runs with different number of MPI processes, each using a single OpenMP thread, which is the configuration with the smallest total time (factorization + solution of 500 rhs). We show the speedup of the factorization phase, the solution phase with 500 rhs, and of both of the phases together.

the model, takes about 4 per cent of the forward modelling time for a model with a mesh 101x 101y 50z and 256 MT receivers.

5 DIRECT SOLVER

Several attractive features of direct solutions were listed in Introduction. Here we investigate the viability of 3-D FE modelling and inversion performed on single-chassis, multicore, SMP computers typically used in server applications and which are relatively affordable. We were attracted to this platform at first for direct solution of the model-space, Gauss–Newton parameter step equation, which was parallelized using a matrix tiling approach under OpenMP compiler directives and showed good scalability across an 8-core workstation with 32 GB RAM (Maris & Wannamaker 2010). Initially this tiling solution was applied also to the banded (daSilva *et al.* 2012) FE matrix and showed good scalability across a newer 24-core workstation with 512 GB RAM (Kordy *et al.* 2013). However, solution time overall was slower than desired, for example taking over 1 hr per frequency for a mesh 85x 88y 50z and two source vectors (i.e. no Jacobians).

Thus, in an effort to improve speed, we have investigated two popular computational libraries for directly factorizing $A = LDL^T$ and reducing source vectors. One is MUMPS (Amestoy *et al.* 2001, 2006), utilized by others (e.g. Oldenburg *et al.* 2008; Streich 2009; daSilva *et al.* 2012; Oldenburg *et al.* 2013). The other is PARDISO (Intel MKL implementation) (Schenk & Gärtner 2004). PARDISO has turned out to be faster in a shared memory setting.

The matrix A in eq. (9) is complex valued and symmetric (but not Hermitian). Both solvers initially find a permutation of variables, P, and the matrix is replaced with PAP^T (permutation of both columns and rows of the matrix, so that the matrix remains symmetric). Then a lower triangular matrix L and a diagonal matrix D are found such that $PAP^T = LDL^T$. The last step is the solve phase, that is, solving the system (8), which may be written as

$$PAP^T(P\xi) = Pb \quad \text{or} \quad LDL^T\tilde{\xi} = Pb, \quad \text{where} \quad \tilde{\xi} = P\xi$$

Permutation P is chosen to minimize the number of nonzero values in L matrix, and to allow for parallelization of the factorization and solve phases.

Both MUMPS and MKL PARDISO use third party ordering libraries to find P. For a comparison of the two solvers, we used the METIS (Karypis 2003) ordering library and thus both MUMPS

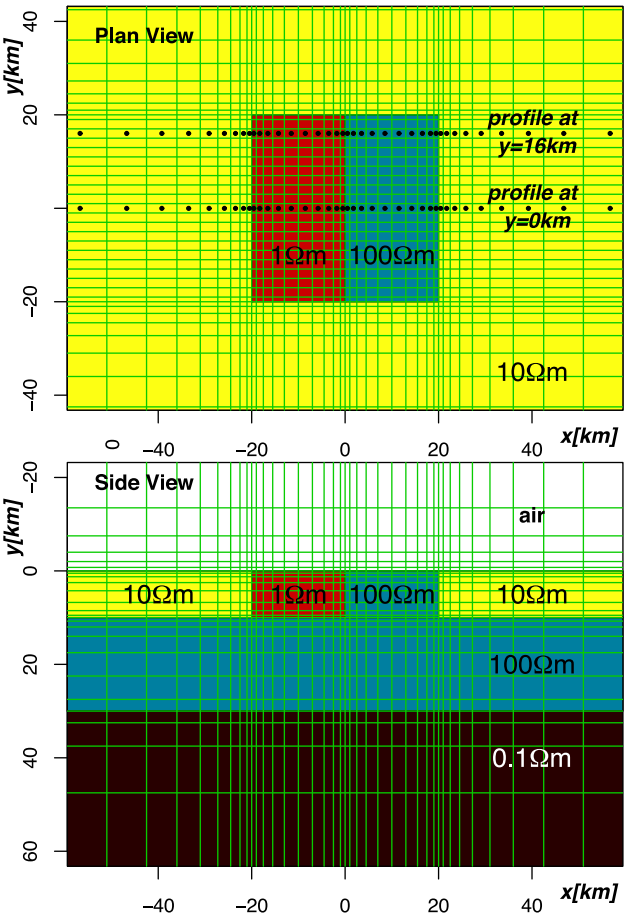

Figure 4. Outcropping double brick resistivity model, together with the mesh used. Element boundaries are drawn as solid green lines.

and PARDISO calculate L having the same number of non-zeros. For a mesh with 85x 85y 90z cells, on a 24-core workstation (four Intel E5-4610 Sandy Bridge hex-core processors at 2.4 GHz), the factorization time of matrix (9) with MKL PARDISO was typically ∼40 per cent of that of MUMPS. The solution phase of MKL PARDISO took about 80 per cent of that of MUMPS. This may reflect the fact that PARDISO is written for the shared memory architecture (although there is an option to use it on a cluster), whereas

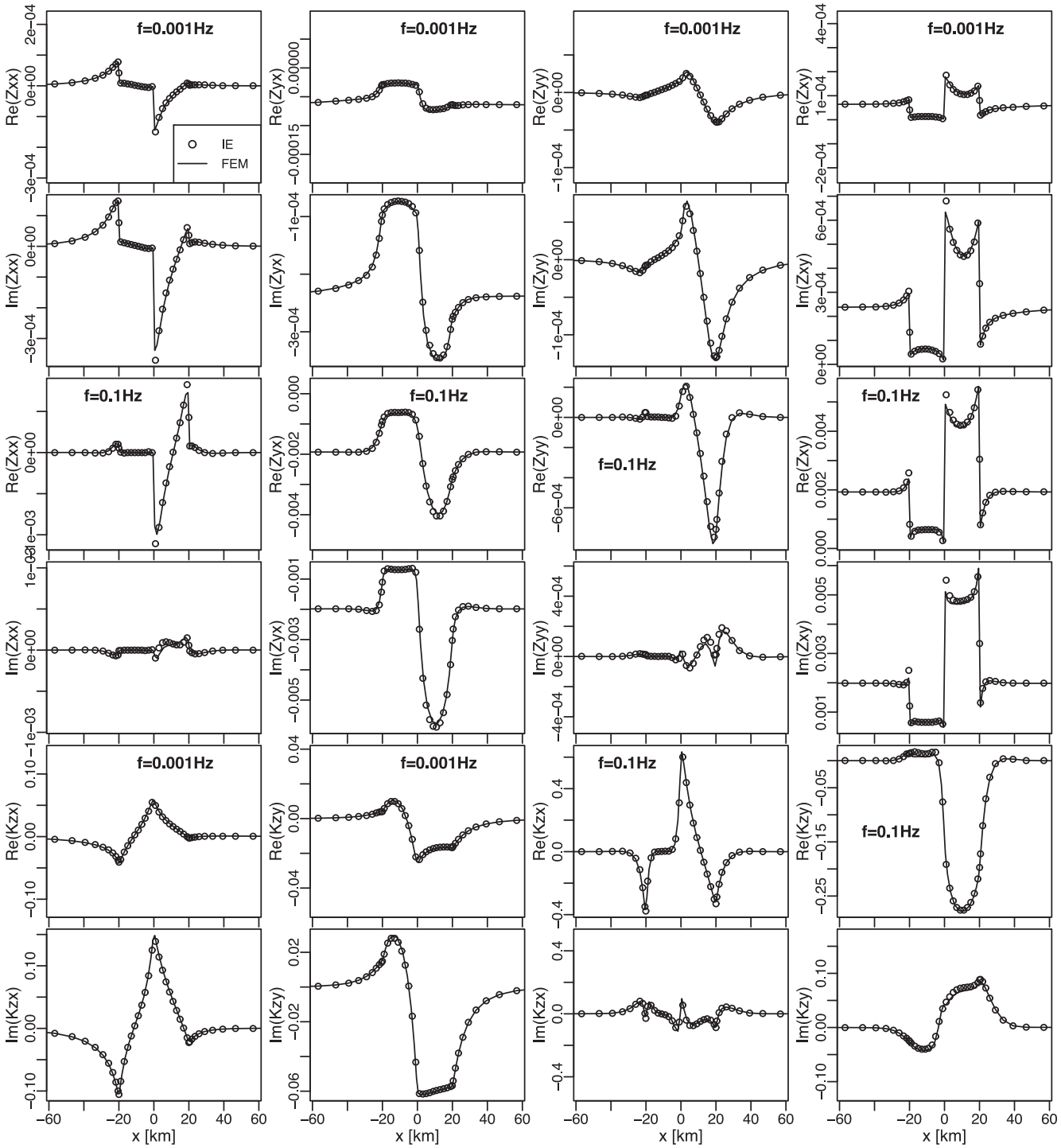

Figure 5. Forward MT response of a double brick model for profile at $y = 16$ km for comparison with Integral Equation code response. Frequencies are 0.001 and 0.1 Hz.

MUMPS is written for a distributed memory system. Additionally MUMPS uses more memory if many MPI processes are used, as the data are copied between the processes. MUMPS with 24 MPI processes uses more than twice the memory than that when run with one MPI process, which is about the amount of memory that MKL PARDISO needs.

The scalability of MKL PARDISO (version 11.2 of MKL library) and MUMPS (version 4.10.0) libraries is presented in Fig. 3. With 24 cores, the speedup of the factorization and solution phases is 18 and 13, respectively for PARDISO. For comparison, the speedup of MUMPS with 24 MPI processes, for the same problem, is 9 and 7 for the factorization and solution phases respectively. Furthermore we found that MUMPS scalability nearly plateaued between 12 and 24 cores. The times of computation for 24 cores were 81 and 111 s for factorization and solution phases in the case of PARDISO, and 190 and 153 s for factorization and solution phases in the case of MUMPS. Performance improvements may be expected in future versions of either library.

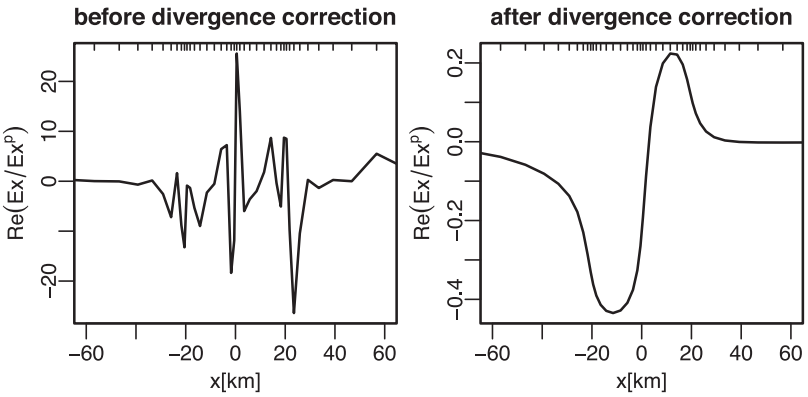

Figure 6. Real component of electric field E_x at a height of 2 km for the double brick model calculated before and after divergence correction for a frequency of 0.001 Hz. *Y*-axis scales are different for figure on the right and on the left; the field before correction is 100 × larger overall in magnitude. Tick marks along top plot border show calculation point locations.

6 EXAMPLE FORWARD CALCULATIONS

The accuracy of our 3-D FE forward code is tested against independent algorithms. These include a standard test of conductive and resistive heterogeneity under a flat surface, but we also focus on topography as a principal rationale for this work. Tests highlight the strength of the FE method in defining smooth, non-jagged topographic slopes.

6.1 Outcropping double brick Model

First we consider the popular, outcropping double brick 3-D model originally proposed in 2-D by Weaver *et al.* (1985, 1986) and included in the Commemi collection of trial models by Zhdanov *et al.* (1997). The central portion of its FE mesh appears in Fig. 4. The mesh has $52x\,53y\,31z$ elements, out of which the two bodies consist of $20x\,21y\,8z$ elements. We used 10 layers for the air and 21 layers for the earth. Element sizes grow steadily away from the centre of the domain to a total distance of 555 km from the centre. The 1-D background model is the true 3-D model without the two outcropping bricks. All calculations are done in double precision.

Complex tensor impedance Z and tipper K elements were calculated at the surface, over the cells' centres, along a profile at $y = 16$ km for frequencies of 0.001 Hz and 0.1 Hz. They are compared in Fig. 5 with those computed using the Integral Equations code of Wannamaker (1991), for which the body discretization coincides with that of the FE mesh. The agreement between the two codes clearly is very good, and compares favourably with the check against a finite difference approach in Mackie *et al.* (1993). Comparison was similarly good for the profile at $y = 0$ km (not shown) although Z_{xx}, Z_{yy}, K_{zy} are zero there.

The requirement for, and effectiveness of, the divergence correction described previously, is demonstrated for a profile 2km in the air over the centre of the double brick model in Fig. 6. On the left is the electric field in the *x*-direction across the sides of the body at the low frequency of 0.001 Hz. It consists mainly of numerical noise due to spurious curl-free electric fields. Nevertheless, as seen on the right side, the divergence correction is able to remove the error leaving a response which is a smooth, upward-continued version of a surface response (*cf.* Z_{xy} in Fig. 5). Thus we are able to model accurate E-fields in the air with our FE method as would be desired under efforts to create airborne MT platforms (e.g. Macnae 2010).

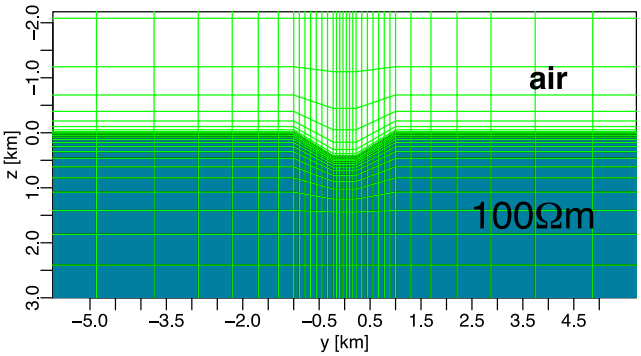

Figure 7. *YZ* cross-section of a 2-D valley, together with the central part of the 3-D FEM mesh. Element boundaries are drawn as solid green lines.

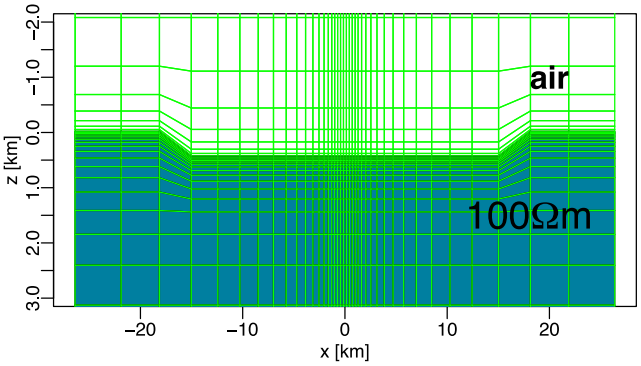

Figure 8. *XZ* cross-section of the 2-D valley, together with the 3-D FEM mesh. 5× vertical exaggeration.

6.2 2-D valley and hill

Because topographic simulation and inversion is a principal motivation for this work, we present several accuracy checks here. First, we compare fields over an elongate 3-D valley with those of the 2-D valley model of Wannamaker *et al.* (1986) computed with their nodal FE code. The valley is 450 m deep, 500 m wide at the bottom and 3 km wide at the top in a host of resistivity $\rho = 100\,\Omega$m (3-D cross-section in Fig. 7). In 3-D, infinite strike is approximated with a 30 km length (Fig. 8). The entire 3-D mesh consisted of $39x\,41y\,30z$ elements while the valley portion was covered by 21 elements across the *y*-direction. The mesh extended to 6 km above the ground, 11 km below the ground and laterally 26 km and 14 km from the valley

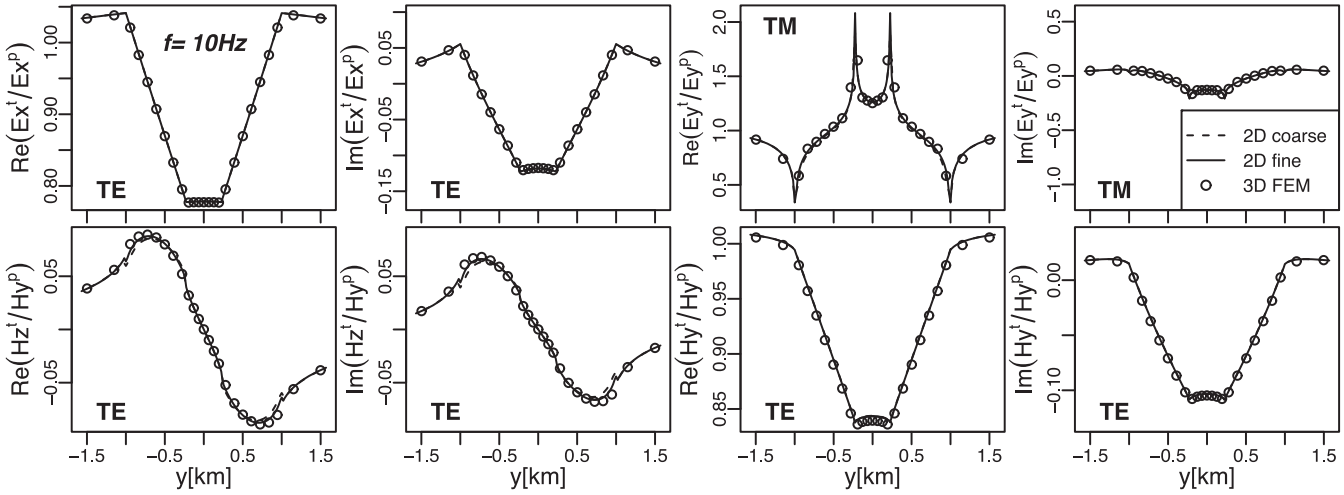

Figure 9. Normalized EM fields along the profile across the 2-D valley, for $x = 0$ km.

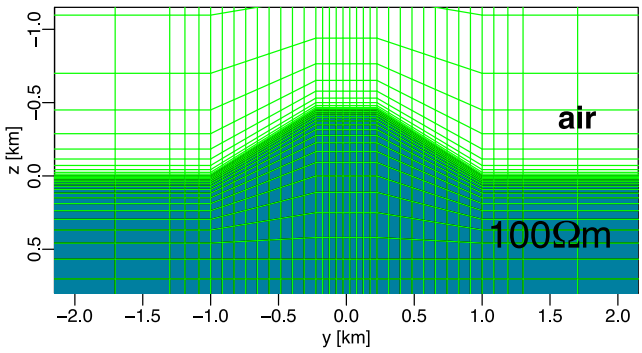

Figure 10. *YZ* cross-section of a 2-D hill, together with the central part of 3-D FEM mesh.

in *x*- and *y*-directions respectively. The 1-D background model is a 100 Ωm half space.

A coarse and a finer 2-D discretization are considered. The coarse valley is made up of 20 layers of elements each 22.5 m thick. The finer valley is made up of 40 layers of elements each 11.25 m thick. Element dimensions grow steadily away from the centre to a total distance of over 20 km to the sides and depth. Note that the 2-D mesh is rectilinear such that slopes must be made up of triangles rather than deformed quadrilaterals (Wannamaker *et al.* 1986). The *E*- and *H*-fields across the valley centre normalized by the primary fields are plotted in Fig. 9. The responses of the 3-D and 2-D codes are in close agreement.

For the hill model, we consider the high frequency of 1000 Hz to test whether the 3-D code can accurately simulate refraction of the EM fields normal to the slope, as was done in 2-D by Wannamaker *et al.* (1986). The small skin depth (∼160 m) requires a finer mesh

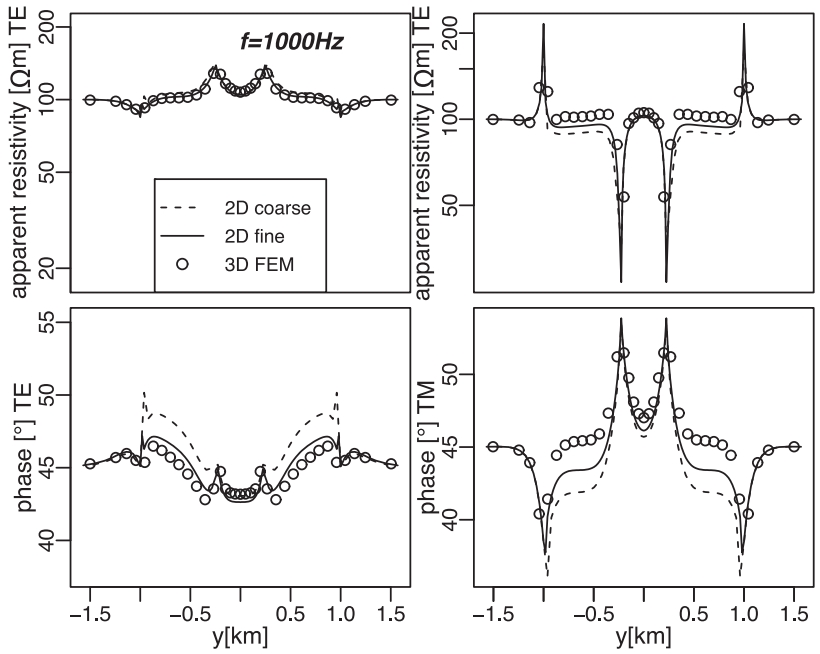

Figure 11. The ρ_a and phase responses from the 2-D code and 3-D codes for the 2-D hill at 1000 Hz. TE denotes the values derived from Z_{xy}, TM denotes the values derived from Z_{yz}.

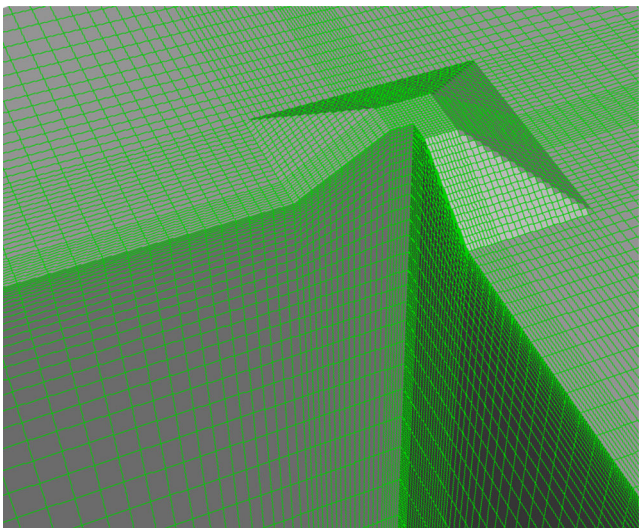

Figure 12. Central part of the finer mesh for the 3-D hill model.

closer to the hill surface, although the lateral limits do not have to be so far (Fig. 10). The mesh extends 3 km above the highest point, 1.3 km below the base and laterally 5 and 4 km from the hill in x- and y-directions. The 2-D hill has the same dimensions and discretization as the valley for both coarse and fine versions. We compute the E- and H- fields parallel to the slope of the hill, and use those values to calculate apparent resistivity ρ_a.

The ρ_a should approach the true resistivity of the ground (100 Ωm) at high frequency because the total EM fields ideally become purely parallel to the slope. We present ρ_a and phase for TE and TM modes in Fig. 11. Note that for both fine mesh 2-D code and 3-D code results, away from breaks in slope, ρ_a is close to 100 Ωm and phase is close to 45°. In fact, the 3-D phase results look the most accurate, which may reflect a greater ease for layers of hexahedral elements to simulate essentially 1-D fields than for triangles, although the 2-D results are converging with finer discretization.

6.3 3-D trapezoidal hill

The next test model is the 3-D hill model considered by Nam *et al.* (2007). It has the same dimensions as the previous 2-D hill, but is square in horizontal cross-section (see Fig. 12). It is 0.45 km high, 0.5 km wide at the hilltop, 2 km wide at the base with resistivity of 100 m. It is calculated for 2 Hz, and the MT response is compared to that of Nam *et al.* (2007) and Ren *et al.* (2013). The background 1-D model is a 100 Ωm half space. Two grids were considered, the finer grid being 97x, 97y, and 50z while the coarser grid is 27x, 27y, 24z. The ρ_a, phase and the tipper along a profile across the centre of the hill are presented in Figs 13 and 14. The MT response calculated in Nam *et al.* (2007), Ren *et al.* (2013) and the field calculated by our FE code appear very similar.

6.4 Mount Erebus volcanic edifice, Antarctica

The prior topographic models involve relatively simple shapes and slopes. To test our algorithm's ability to accurately simulate topographic response of a complex natural structure, we consider Mount Erebus on Ross Island, Antarctica. Rising from sea level to 3794 m elevation, it may be the best example of an active phonolitic volcano (Moussallam *et al.* 2013). Our group has begun a comprehensive

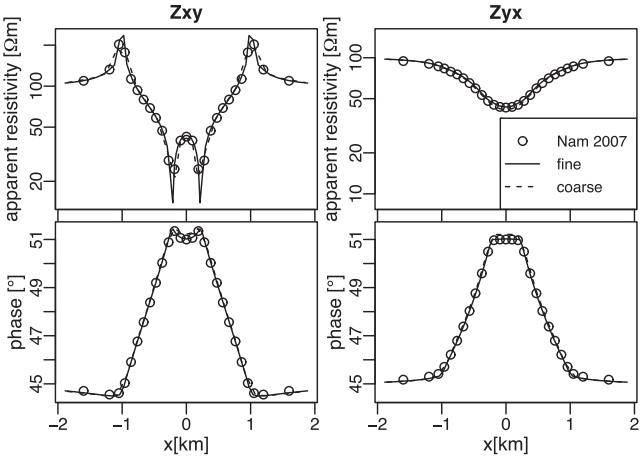

Figure 13. Apparent resistivities and phases for the 3-D hill model along a profile across the hill compared with the result of Nam *et al.* (2007). The results of Nam have been discretized from their plots.

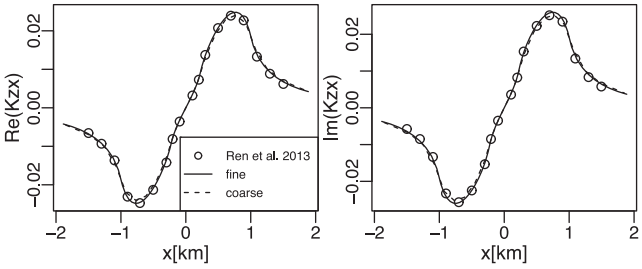

Figure 14. Tipper (x-component) for the 3-D hill model along a profile across the hill compared with the result of Ren *et al.* (2013) calculated on their seventh mesh. The results of Ren *et al.* have been discretized from their plots and converted to $e^{i\omega t}$ time dependence.

3-D MT field survey to verify petrological models for magma genesis and transport (Hill *et al.* 2015). One season of fieldwork has been completed in 2014–2015, with two more consecutive seasons mobilizing at the time of this writing. Final responses are to be available for modelling in mid-2017. All sites are placed by helicopter assist, enabling relatively uniform coverage even in steep terrain. The digital elevation model (DEM) for Ross Island and surrounding bathymetry was provided by the New Zealand GNS Science organization at 40 m lateral spacing and ±6 m vertical accuracy from the resource described in Csatho *et al.* (2008) and the Ross Sea map of Davey (2004).

The main test is one of convergence with discretization, which involves three aspects. The first is convergence of MT response with mesh discretization for a fixed topographic geometry. The second is convergence of the subsampled topography towards the true surface with finer meshing. The third is convergence of computed response as mesh receiver location approaches true receiver location with discretization. As noted previously, mesh receivers are placed over element centres consistent with the fact that a single magnetic flux is estimated from $\nabla \times E$ around cell edges; this is standard both for first order Nédélec elements and for staggered grid finite difference methods (e.g. Madden & Mackie 1989; Mackie *et al.* 1993; Siripunvaraporn *et al.* 2002).

We consider five meshes, where mesh 1 is the coarsest (35x 52y 26z) and mesh 5 is the finest (127x 193y 101z) (Fig. 15; the intermediate mesh 3 is shown in Fig. 1). At each step, the mesh is refined by a factor of $\sqrt{2}$, so that in two steps the mesh is refined by a factor of 2. The location of the receiver on each mesh is the face

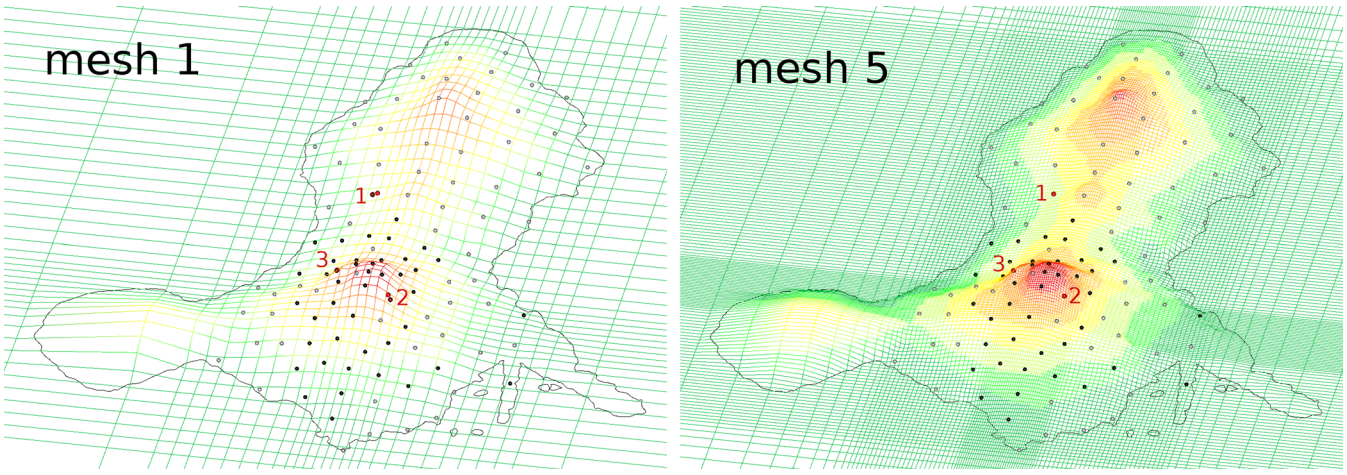

Figure 15. Meshes 1 and 5 for Mount Erebus model. Black dots show the locations of MT data collected to date, while grey dots are planned locations. Three light red dots show the true location of receivers for which MT responses are considered here. Dark red dots are the location of the closest surface face centre, where the fields are calculated.

centre closest to the true receiver location. The steep cone of Mount Erebus has the elements with the smallest x and y extent, the rest of Ross Island has its elements up to two times larger, and around the island the elements grow at a constant geometrical rate to reach the boundary of the domain which is 500 km away. The bottom and the top of the domain are at ±500 km distance from sea level. Bathymetry around the island is included to a distance of ∼200 km whereupon it is terminated, although seawater depths are only a few hundred meters until several kilometres from the shoreline. Additionally for each mesh, the elevation of the surface vertices was calculated as an average of the DEM on an area comparable to the horizontal extent of the element. As a result, the topography represented on a mesh converges towards the true topography as the mesh gets finer.

The Mount Erebus model is given a uniform resistivity of 100 Ωm in order to illustrate the effects of topography and meshing. Although it is difficult to isolate the three prior issues, if responses from all five meshes are reasonably close and converge with discretization, then our approach to modelling natural topography should be robust. We consider three MT receivers in Fig. 15 whose local slope is 7–8°, 28–25° and 32–40° respectively from meshes 1–5. Sites 1 and 2 are actual survey locations; 2 in particular required picketed roped travel from the landing spot and is the steepest of the project. Site 3 is hypothetical and considered inaccessible, and so should be a limiting test. The complex impedance and tipper elements are plotted in Fig. 16. For plotting, the impedance Z_k is normalized relative to that at mesh 5 according to

$$\tilde{Z}_k(i,j,l,m) = \frac{Z_k(i,j,l,m)}{\frac{1}{2}|Z_5(1,2,l,m) - Z_5(2,1,l,m)|} \tag{28}$$

for $i = 1, 2$ $j = 1, 2$ for mesh k, receiver l and frequency m. The denominator in eq. (28) is the impedance invariant for mesh 5.

Fig. 16 shows good agreement across meshes and good convergence of the MT responses with mesh refinement. As a measure of error, a relative difference (RD) between the responses from mesh k and mesh 5 is computed in a normalized root-mean-square fashion:

$$\mathrm{RD}(k,5) = \sqrt{\frac{1}{12 N_{\mathrm{rec}} N_{\mathrm{freq}}} \sum_{l=1}^{N_{\mathrm{rec}}} \sum_{m=1}^{N_{\mathrm{freq}}} R^2_{l,m}} \tag{29}$$

where

$$R^2_{l,m} = \sum_{i=1}^{2}\sum_{j=1}^{2} \left|\tilde{Z}_k(i,j,l,m) - \tilde{Z}_5(i,j,l,m)\right|^2 + \sum_{j=1}^{2} \left|K_k(j,l,m) - K_5(j,l,m)\right|^2$$

Values of RD are listed in Table 1. With mesh refinement, the topography changes and the receivers shift modestly. This may be degrading the order of convergence slightly, which shows a value of about 0.8 instead of the ideal 1. Nevertheless, the relative differences are small compared to typical error floors adopted in 3-D inversion, for example 5 per cent on the impedance elements by Meqbel *et al.* (2014). This is achieved even for the receiver where local slope reaches 40 degrees.

As a second test, in Appendix B we present the results of a high frequency test similar to the one of Fig. 11 for the 2-D hill. For each receiver, we rotate the coordinate system such that the X and Y axes are parallel to the slope and the Z axis is perpendicular to the slope and calculate the MT response in those coordinates. We observe that as frequency increases, the apparent resistivity approaches 100 Ωm, the phase approaches 45°, and the tipper components approach 0 as should be expected. Note that the on-diagonal impedance elements in Fig. 16 also approach zero towards high frequency. The asymptotes occur near 100 Hz, above which results begin to diverge, although this is near the highest frequency usefully interpreted for a survey of this scale. We might expect further modest mesh changes as the project progresses, but these results demonstrate the efficacy of our approach to topographic modelling.

6.5 Jacobians test calculations

Next, we test the calculation of MT response Jacobians as they are essential for inversion purposes. We consider derivatives with respect to $\log_{10}$ resistivity model $m = (m_j)_{j=1}^{N_m}$, where in principle each m_j could be parsed as finely as a single FE. We consider the coarse 3-D hill mesh with receivers over the centres of surface element faces at $y = 0$ km. For the test parameter we use two adjacent FEs on the facing hill slope (Fig. 17). Jacobians are calculated using

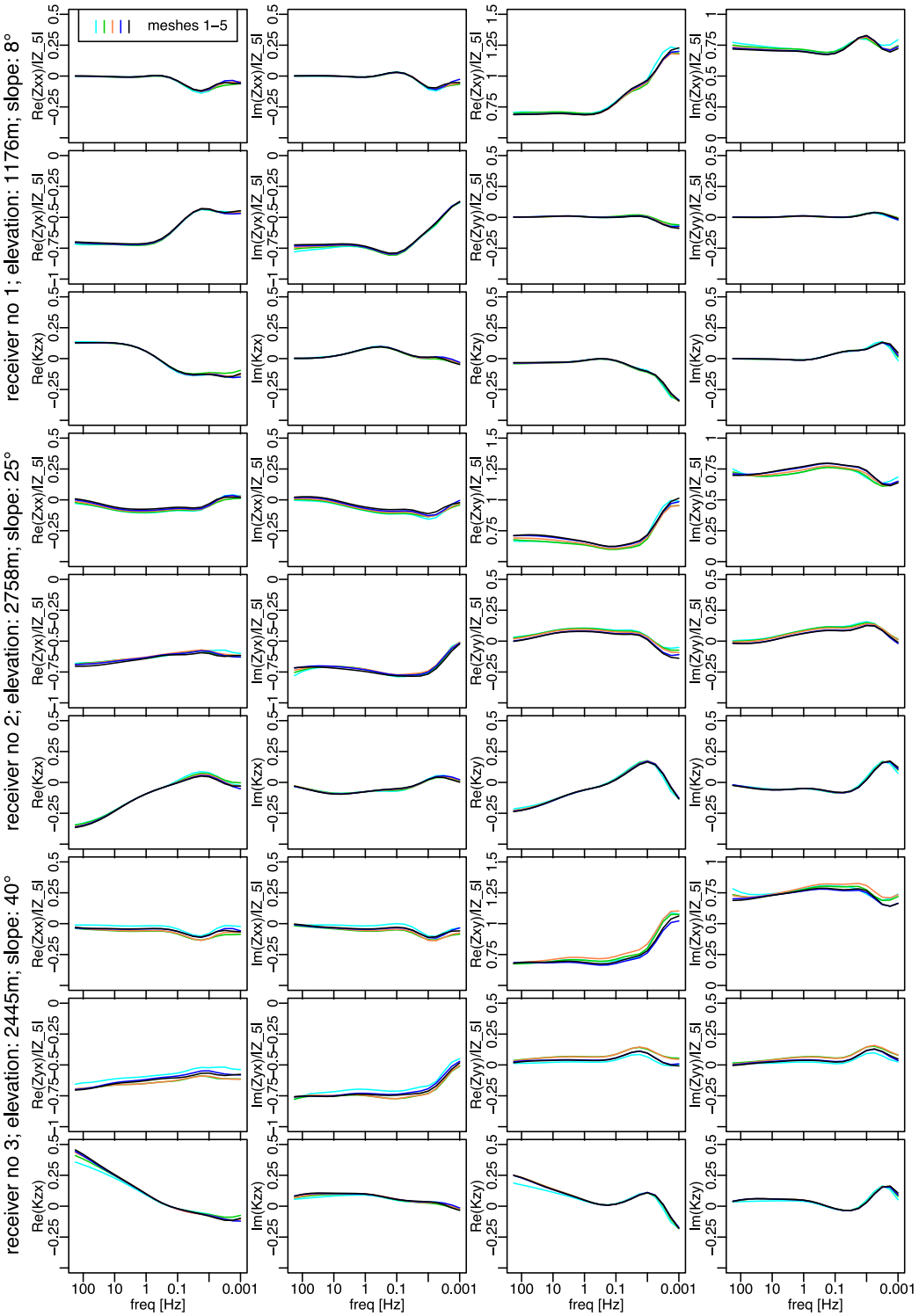

Figure 16. Normalized impedance $\tilde{Z}$ (eq. 28) and tipper K as a function of frequency for three receivers of the Mount Erebus model. The denominator in eq. (28) is abbreviated here as $|Z\_5|$.

Table 1. Comparison of the response of mesh k with the response of the finest mesh 5 for the three receivers together and separately using eq. (29).

	RD(1,5)	RD(2,5)	RD(3,5)	RD(4,5)
All 3 recs	2.36%	1.89%	1.69%	0.79%
rec 1	2.62%	2.28%	1.69%	0.88%
rec 2	1.5%	1.17%	0.7%	0.63%
rec 3	2.75%	2.04%	2.29%	0.85%

reciprocity as described previously and they are compared with a symmetric difference approximation of the derivative, that is,

$$\frac{\partial(Z,K)}{\partial m_j}(m) \approx \frac{(Z,K)(m+e_j h)-(Z,K)(m-e_j h)}{2h}$$

where e_j is a vector with only one nonzero entry at the jth position, which is equal to 1. In Fig. 18, we present the result of calculation for

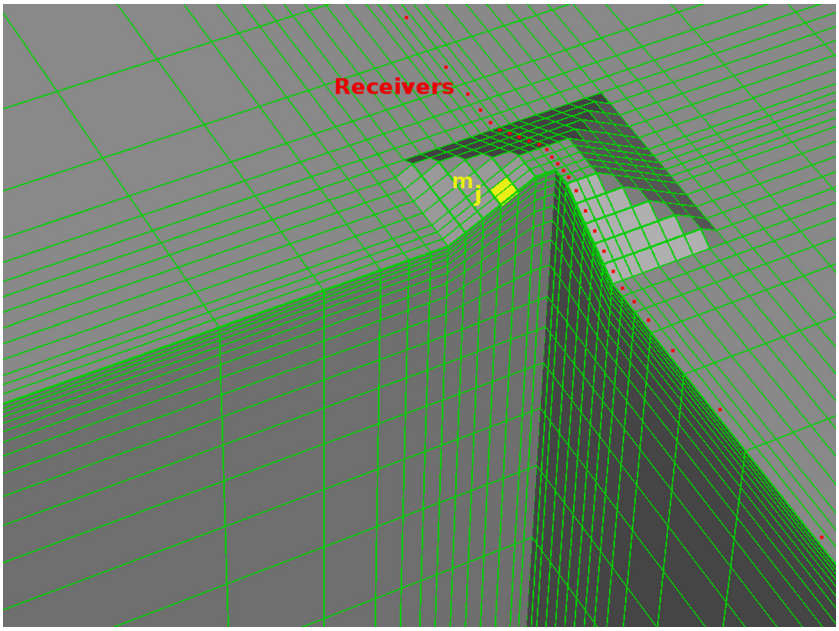

Figure 17. Central part of the coarse mesh of 3-D hill, together with the location of receivers and the chosen inversion cell m_j.

frequencies of 100 Hz and 0.001 Hz for all components of Z, K and for the inversion cell marked in the model figure. We used $h = 0.05$. A wide range of frequencies and various locations of the inversion cell have been tried, including the location under the receiver line. In all cases the values of the Jacobians showed very close agreement, with the relative difference no more than 0.2 per cent for non-zero components of the Jacobian.

7 EXAMPLE RUN TIMES

In Tables 2 and 3, we present run times related to solving eq. (8) with the MKL PARDISO library. Those run times constitute the main computational time of the forward modelling. For a model with a mesh $101x\,101y\,50z$ and 256 MT receivers other calculations (the calculation of the system matrix A and the source vectors b, sparse calculations related to divergence correction and the evaluation of the Jacobian, once the solutions $A^{-1}w$ are obtained) take about 13 per cent of the forward modelling time. The calculations were done on a 24 core workstation (four Intel Xeon E5-4607 v2 Hexa-core 2.60 GHz processors). Recall that MKL PARDISO finds a permutation matrix P (reordering phase), then calculates matrices L, D such that $P^TAP = LDL^T$ (factorization phase). Then L and D are used to solve linear system (8) for numerous rhs vectors b.

Times in the tables correspond to work done for a single frequency. In order to calculate full MT Jacobians, for each receiver location one needs to solve five linear systems (8). For example, 500 rhs in Table 3 would correspond to a survey with 100 receivers. As expected, run-time increase is geometric with respect to number of unknowns. In Table 2 we present the reordering time, which is about 10 times less than the factorization time with 24 cores. Here it is calculated using the sequential library METIS, which we found to be stable. METIS uses only one core; thus on a machine with more cores, the reordering time will become more significant. However, since reordering depends only on the non-zero pattern of the matrix and not on entry values, reordering is the same for every frequency so it may be reused for all frequencies following the first.

With a data-space parameter step formulation, as discussed in Part II, the inversion run time will be dominated by the forward problem and Jacobians. For the largest test mesh of Table 2 and assuming each element can be a parameter, a regular 400 site survey (20×20) could be inverted using a mesh with six columns of parameters per site in both x- and y-directions leaving nearly 30 columns of padding to far distances outside the survey domain.

8 CONCLUSIONS

FEs provide a flexible and accurate means of simulating EM responses of 3-D resistivity structure beneath topographic variations. Hexahedral elements provide a straightforward means of representing earth surface slopes, are compatible with the Helmholtz governing equation as discretization increases, and generate FE system matrices of simple structure. In particular, discretization requirements for topography at high frequencies are modest compared to those for traditional rectilinear meshes because layers of elements can lie parallel to the earth's surface. Further research is warranted into element discretization and geometry, applications for bathymetry and seafloor responses, and more complex background structures. By invoking an efficient current divergence correction, accurate E-field results may be obtained at very low frequencies and small admittivities, even those of dielectric air. Because we utilize a secondary field approach, it should be straightforward to generalize to finite source problems. As will be shown in Part II, hexahedral elements also provide a simple path to regularized inversion, for example by direct mapping of triaxial parameter roughness damping into deformed coordinates.

Efficient and affordable parallel computing solutions have emerged that are putting direct solutions to fairly large 3-D EM simulation problems within reach of an increasing number of users. These include a powerful public-domain library for direct solutions (MUMPS) that is seeing increased community use or a commercial library MKL PARDISO as exploited in this paper. Because the factorization provided by direct solvers allows economical solution

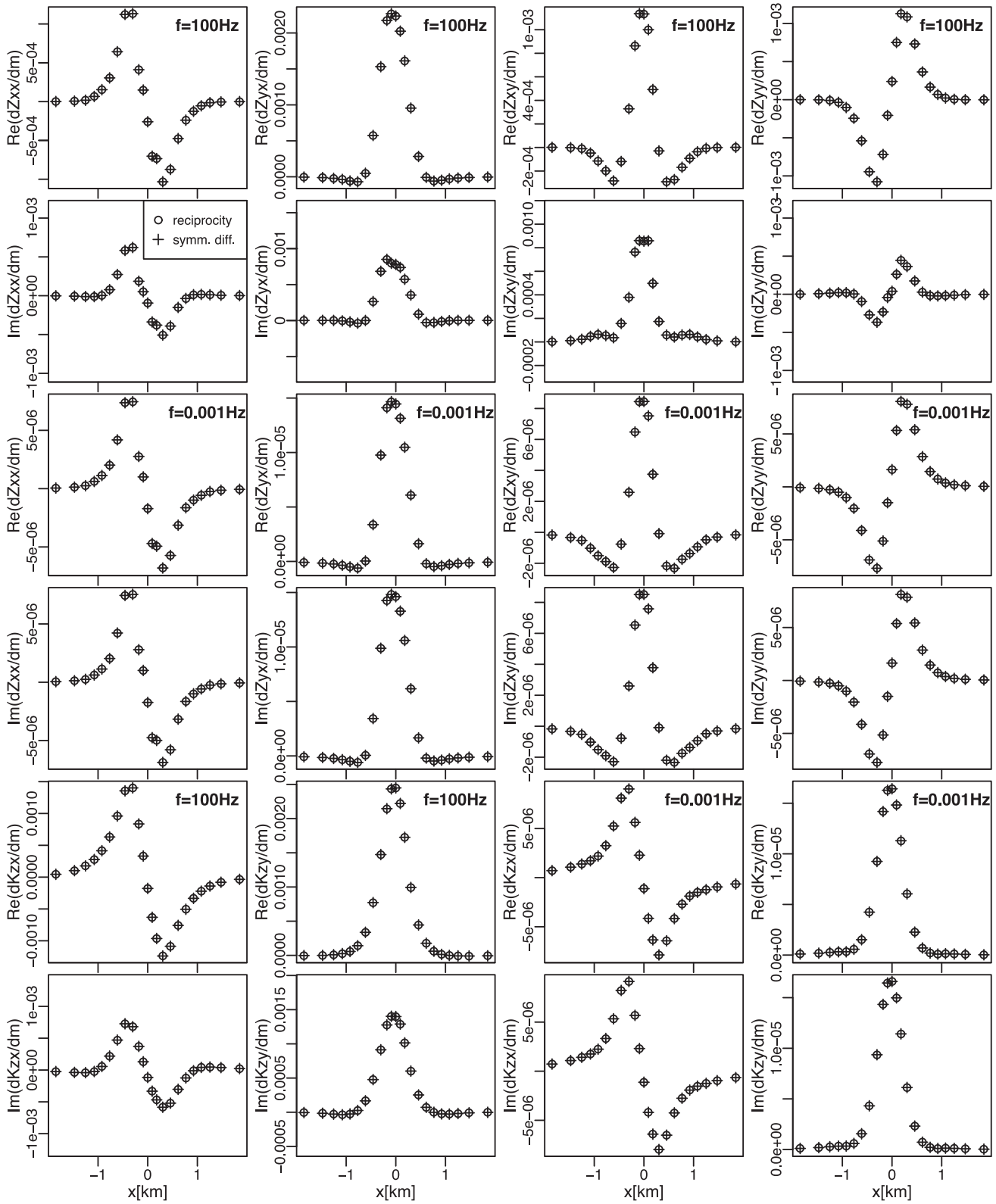

Figure 18. Comparison of a Jacobian of Z, K calculated using reciprocity and symmetric difference. The relative difference between the plotted values is less than 0.1 per cent.

of large numbers of source vectors, explicit and accurate values of parameter Jacobians can be obtained. Technological advances also include single-box, server-class workstations with numerous cores and substantial RAM that provide relatively affordable computing. Parallelization of the direct solver MKL PARDISO on multicore SMP computers is good, reaching an overall speedup of 15 on a 24 core machine for the forward problem calculations. Parallelization also could be increased with distributed computing using multiple

Table 2. MKL PARDISO analysis and factorization phase times (in min:sec) for factoring matrix A in eq. (8) for various meshes.

Mesh	Number of unknowns A	Number of non-zeroes in A	Number of non-zeroes in L	Reordering time	Factorization time	RAM memory used (GB)
30x 30y 25z	62 785	1 008 965	24 225 432	00:01	00:01	0.68
50x 50y 35z	250 635	4 111 215	180 177 821	00:05	00:13	4.17
75x 75y 45z	734 820	12 179 490	770 644 591	00:17	01:00	14.55
100x 100y 50z	1 460 250	24 316 190	1 981 092 177	00:37	03:48	35.09
125x 125y 55z	2 519 680	42 085 390	4 135 494 960	01:08	10:55	70.41
150x 150y 60z	3 969 360	66 443 340	7 022 172 676	01:53	21:03	117.10
176x 176y 70z	6 394 150	107 274 730	14 344 449 730	03:18	64:10	233.80

Table 3. MKL PARDISO solution phase time (in min:sec) for the linear system (8), for various meshes and numbers of rhs vectors b.

Mesh	100 rhs	500 rhs	1000 rhs	1500 rhs	2000 rhs
30x 30y 25z	00:01	00:03	00:07	00:10	00:13
50x 50y 35z	00:02	00:11	00:23	00:34	00:45
75x 75y 45z	00:11	00:54	01:48	02:42	03:36
100x 100y 50y	00:05	00:23	00:46	01:10	01:33
125x 125y 55z	01:24	06:58	13:57	20:55	27:53
150x 150y 60z	02:09	10:47	21:34	32:22	43:09
176x 176y 70z	03:41	18:23	36:47	55:10	73:34

SMP. Nevertheless, direct simulations including Jacobians can be done on a single workstation for meshes with one million elements in less than 1 hr per frequency.

ACKNOWLEDGEMENTS

We acknowledge the support for this work from the U.S. Department of Energy under contract DE-EE0002750 and the U.S. National Science Foundation under grant AES-1443522 to PW. EC acknowledges the partial support of the U.S. National Science Foundation through grants ARC-0934721 and DMS-1413454. GH acknowledges the support of the Royal Society of New Zealand through grant ASL-1301. The University of Utah/EGI funded acquisition of the 24-core workstations. Drs. Rita Streich and Martin Čuma are thanked for discussions on libraries for direct solutions of sparse systems. Belinda Lyttle of the New Zealand GNS Science organization kindly provided the Ross Island and surroundings DEM. Presentation and content of the paper were improved substantially following the remarks of three anonymous reviewers. The submission was handled by Associate Editor Ute Weckmann.

REFERENCES

Adams, R. & Fournier, J., 2003. *Sobolev Spaces,* Elsevier Science.

Amestoy, P.R., Duff, I.S., Koster, J. & L'Excellent, J.-Y., 2001. A fully asynchronous multifrontal solver using distributed dynamic scheduling, *SIAM J. Matrix Anal. Appl.,* **23**(1), 15–41.

Amestoy, P.R., Guermouche, A., L'Excellent, J.-Y. & Pralet, S., 2006. Hybrid scheduling for the parallel solution of linear systems, *Parallel Comput.,* **32**(2), 136–156.

Amrouche, C., Bernardi, C., Dauge, M. & Girault, V., 1998. Vector potentials in three-dimensional non-smooth domains, *Math. Methods Appl. Sci.,* **21**(9), 823–864.

Börner, R.-U., 2010. Numerical modelling in geo-electromagnetics: advances and challenges, *Surv. Geophys.,* **31,** 225–245.

Börner, R.-U., Ernst, O.G. & Spitzer, K., 2008. Fast 3D simulations of transient electromagnetic fields by model reduction in the frequency domain using Krylov subspace projection, *Geophys. J. Int.,* **173,** 766–780.

Chave, A.D. & Jones, A.G., 2012. *The Magnetotelluric Method: Theory and Practice,* Cambridge Univ. Press.

Commer, M. & Newman, G.A., 2008. New advances in three-dimensional controlled-source electromagnetic inversion, *Geophys. J. Int.,* **172,** 513–535.

Csatho, B., Schenk, T., Kyle, P., Wilson, T. & Krabill, W.B., 2008. Airborne laser swath mapping of the summit of Erebus volcano, Antarctica: applications to geological mapping of a volcano, *J. Volc. Geotherm. Res.,* **177**(3), 531–548.

daSilva, N.V., Morgan, J.V., MacGregor, L. & Warner, M., 2012. A finite element multi-frontal method for 3D CSEM modeling in the frequency domain, *Geophysics,* **77,** E101–E115.

Davey, F.J., 2004. *Ross Sea bathymetry,* Institute of Geological & Nuclear Sciences, Geophys. Map 1172-0301, 1:2,000,000.

deGroot-Hedlin, C. & Constable, S., 1990. Occam's inversion to generate smooth, two-dimensional models from magnetotelluric data, *Geophysics,* **55**(12), 1613–1624.

deLugao, P.P. & Wannamaker, P.E., 1996. Calculating the two-dimensional magnetotelluric Jacobian in finite elements using reciprocity, *Geophys. J. Int.,* **127,** 806–810.

Everett, M.E., 2012. Theoretical developments in electromagnetic induction geophysics with selected applications in the near-surface, *Surv. Geophys.,* **33,** 29–63.

Falk, R.S., Gatto, P. & Monk, P., 2011. Hexahedral H (div) and H (curl) finite elements, *ESAIM: Math. Modelling Numer. Anal.,* **45**(01), 115–143.

Farquharson, C.G. & Miensopust, M., 2011. Three-dimensional finite-element modeling of magnetotelluric data with a divergence correction, *J. Appl. Geophys.,* **75,** 699–710.

Girault, V. & Raviart, P.-A., 1986. *Finite Element Methods for Navier-Stokes Equations: Theory and Algorithms,* Springer.

Grayver, A.V., Streich, R. & Ritter, O., 2013. Three-dimensional parallel distributed inversion of CSEM data using a direct forward solver, *Geophys. J. Int.,* **193,** 1432–1446.

Gunzburger, M.D. & Bochev, P.B., 2009. *Least-Squares Finite Element Methods,* Springer.

Haber, E., Ascher, U., Aruliah, D. & Oldenburg, D., 2000. Fast simulation of 3D electromagnetic problems using potentials, *J. Comput. Phys.,* **163**(1), 150–171.

Haber, E., Oldenburg, D.W. & Shekhtman, R., 2007. Inversion of time domain three-dimensional electromagnetic data, *Geophys. J. Int.,* **171**(2), 550–564.

Hill, G.J., Wannamaker, P.E., Wallin, E.L., Unsworth, M.J., Stodt, J.A. & Ogawa, Y., 2015. The Mount Erebus (Ross Dependency – Antarctica) magmatic system from surface to source: insights from magnetotelluric

measurements, in *NZARI Antarctic Science Conference 'Antarctica - A Changing Environment',* June 29–July 2, Christchurch, New Zealand.

Hohmann, G.W., 1988. Numerical modeling for electromagnetic methods of geophysics, in *Electromagnetic Methods in Applied Geophysics — Theory,* vol. 1, pp. 313–363, ed Nabighian, M.N., Society of Exploration Geophysicists, Tulsa, OK.

Hohmann, G.W. & Raiche, A.P., 1988. Inversion of controlled-source electromagnetic data, in *Electromagnetic Methods in Applied Geophysics—Theory,* vol. 1, pp. 469–503, ed. Nabighian, M.N., Society of Exploration Geophysicists, Tulsa, OK.

Hyman, J.M. & Shashkov, M., 1999. Mimetic discretizations for Maxwell's equations, *J. Comput. Phys.,* **151**(2), 881–909.

Jahandari, H. & Farquharson, C.G., 2014. A finite-volume solution to the geophysical electromagnetic forward problem using unstructured grids, *Geophysics,* **79,** E287–E302.

Karypis, G., 2003. Multi-constraint mesh partitioning for contact/impact computations, in *Proc. SC2003,* Phoenix, AZ, ACM.

Key, K. & Constable, S., 2011. Coast effect distortion of marine magnetotelluric data: insights from a pilot study offshore northeastern Japan, *Phys. Earth planet. Inter.,* **184,** 194–207.

Kordy, M., Maris, V., Wannamaker, P. & Cherkaev, E., 2013. 3D edge finite element solution for scattered electric field using a direct solver parallelized on an SMP workstation, in *5th International Symposium on Three-Dimensional Electromagnetics,* Sapporo, May 7–9, p. 4.

Kordy, M., Cherkaev, E. & Wannamaker, P., 2015a. Variational formulation for Maxwell's equations with Lorenz gauge: existence and uniqueness of solution, *Int. J. Numer. Anal. Model.,* **12**(4), 731–749.

Kordy, M., Wannamaker, P., Maris, V., Cherkaev, E. & Hill, G.J., 2015b. Three-dimensional magnetotelluric inversion including topography using deformed hexahedral edge finite elements and direct solvers parallelized on SMP computers, Part II: Direct data-space inverse solution, *Geophys. J. Int.,* doi:10.1093/gji/ggv411.

Lelièvre, P.G. & Farquharson, C.G., 2013. Gradient and smoothness regularization operators for geophysical inversion on unstructured meshes, *Geophys. J. Int.,* **195,** 330–341.

Liu, J., Brio, M. & Moloney, J., 2009. Overlapping Yee FDTD method on nonorthogonal grids, *J. Sci. Comput.,* **39**(1), 129–143.

Mackie, R.L., Bennett, B.R. & Madden, T.R., 1988. Long-period magnetotelluric measurements near the central California coast: a land-locked view of the conductivity structure under the Pacific Ocean, *Geophys. J. Int.,* **95,** 181–194.

Mackie, R.L., Madden, T.R. & Wannamaker, P.E., 1993. Three-dimensional magnetotelluric modeling using difference equations – theory and comparisons to integral equation solutions, *Geophysics,* **58,** 215–226.

Macnae, J., 2010. Electric field measurements in air, in *80th Annual International Meeting,* Expanded Abstract, SEG, Denver, pp. 1773–1777.

Madden, T.R. & Mackie, R.L., 1989. Three-dimensional magnetotelluric modelling and inversion, *Proc. IEEE,* **77**(2), 318–333.

Maris, V. & Wannamaker, P.E., 2010. Parallelizing a 3D finite difference MT inversion algorithm on a multicore PC using OpenMP, *Comput. Geosci.,* **36**(10), 1384–1387.

McGillivray, P., Oldenburg, D., Ellis, R. & Habashy, T., 1994. Calculation of sensitivities for the frequency-domain electromagnetic problem, *Geophys. J. Int.,* **116**(1), 1–4.

Meqbel, N.M., Egbert, G.D., Wannamaker, P.E., Kelbert, A. & Schultz, A., 2014. Deep electrical resistivity structure of the northwestern U.S. derived from 3-D inversion of USArray magnetotelluric data, *Earth planet. Sci. Lett.,* **402,** 290–304.

Mitsuhata, Y. & Uchida, T., 2004. Three-dimensional magnetotelluric modeling using the $t - \omega$ finite element method, *Geohysics,* **69,** 108–119.

Monk, P., 1992. A finite element method for approximating the time-harmonic Maxwell equations, *Numer. Math.,* **63**(1), 243–261.

Moussallam, Y., Oppenheimer, C., Scaillet, B. & Kyle, P.R., 2013. Experimental phase-equilibrium constraints on the phonolite magmatic system of Erebus Volcano, Antarctica, *J. Petrol.,* **54**(7), 1285–1307.

Nam, M.J., Kim, H.J., Song, Y., Lee, T.J., Son, J.-S. & Suh, J.H., 2007. Three-dimensional magnetotelluric modeling including surface topography, *Geophys. Prospect.,* **55,** 277–287.

Nédélec, J.-C., 1986. A new family of mixed finite elements in $\mathbf{R}^3$, *Numer. Math.,* **50**(1), 57–81.

Newman, G.A. & Alumbaugh, D.L., 2000. Three-dimensional magnetotelluric inversion using non-linear conjugate gradients, *Geophys. J. Int,* **140,** 410–424.

Oldenburg, D.W., Haber, E. & Shekhtman, R., 2008. Forward modeling and inversion of multi-source TEM data, in *78th Annual International Meeting,* Expanded Abstract, SEG, Las Vegas, pp. 559–563.

Oldenburg, D.W., Haber, E. & Shekhtman, R., 2013. Three dimensional inversion of multi-source time domain electromagnetic data, *Geophysics,* **78**(1), E47–E57.

Pridmore, D.F., Hohmann, G.W., Ward, S.H. & Sill, W.R., 1981. An investigation of finite element modeling for electrical and electromagnetic data in three dimensions, *Geophysics,* **46,** 1009–1024.

Ren, Z., Kalscheuer, T., Greenhalgh, S. & Maurer, H., 2013. A goal-oriented adaptive finite-element approach for plane wave 3-D electromagnetic modelling, *Geophys. J. Int.,* **194,** 700–718.

Roy, K.K., 2007. *Potential Theory in Applied Geophysics,* Springer Science & Business Media.

Sasaki, Y., 2001. Full 3-D inversion of electromagnetic data on PC, *J. Appl. Geophys.,* **46,** 45–54.

Schenk, O. & Gärtner, K., 2004. Solving unsymmetric sparse systems of linear equations with PARDISO, *Future Gener. Comput. Syst.,* **20**(3), 475–487.

Schwarzbach, C., 2009. Stability of finite element solutions to Maxwell's equations in frequency domain, *PhD thesis,* Freiberg University of Mining and Technology.

Schwarzbach, C. & Haber, E., 2013. Finite element based inversion for time-harmonic electromagnetic problems, *Geophys. J. Int.,* **193,** 615–634.

Siripunvaraporn, W., Egbert, G. & Lenbury, Y., 2002. Numerical accuracy of magnetotelluric modeling: a comparison of finite difference approximations, *Earth Planets Space,* **54,** 721–725.

Siripunvaraporn, W., Egbert, G., Lenbury, Y. & Uyeshima, M., 2005. Three-dimensional magnetotelluric inversion: data-space method, *Phys. Earth planet. Inter.,* **150,** 3–14.

Smith, J., 1996. Conservative modeling of 3-D electromagnetic fields, Part II: biconjugate gradient solution and an accelerator, *Geophysics,* **61**(5), 1319–1324.

Streich, R., 2009. 3D finite-difference frequency-domain modeling of controlled-source electromagnetic data: direct solution and optimization for high accuracy, *Geophysics,* **74,** F95–F105.

Tarantola, A., 2005. *Inverse Problem Theory and Methods for Model Parameter Estimation,* SIAM.

Trottenberg, U., Oosterlee, C.W. & Schuller, A., 2000. *Multigrid,* Academic press.

Um, E.S., Harris, J.M. & Alumbaugh, D.L., 2012. An iterative finite element time-domain method for simulating three-dimensional electromagnetic diffusion in the earth, *Geophys. J. Int.,* **190,** 871–886.

Um, E.S., Commer, M., Newman, G.A. & Hoversten, G.M., 2015. Finite element modelling of transient electromagnetic fields near steel-cased wells, *Geophys. J. Int.,* **202**(2), 901–913.

Usui, Y., 2015. 3-D inversion of magnetotelluric data using unstructured tetrahedral elements: applicability to data affected by topography, *Geophys. J. Int.,* **202**(2), 828–849.

Vardapetyan, L. & Demkowicz, L., 1999. hp-adaptive finite elements in electromagnetics, Comput. Methods Appl. Mech. Eng., **169**(3), 331–344.

Wannamaker, P., Stodt, J. & Rijo, L., 1986. Two-dimensional topographic responses in magnetotelluric modeling using finite elements, *Geophysics,* **51,** 2131–2144.

Wannamaker, P.E., 1991. Advances in three-dimensional magnetotelluric modeling using integral equations, *Geophysics,* **56,** 1716–1728.

Weaver, J.T., LeQuang, B.V. & Fischer, G., 1985. A comparison of analytic and numerical results for a two-dimensional control model in electromagnetic induction—I. B-polarization calculations, *Geophys. J. R. astr. Soc.,* **82,** 263–277.

Weaver, J.T., LeQuang, B.V. & Fischer, G., 1986. A comparison of analytic and numerical results for a two-dimensional control model in

electromagnetic induction—II. E-polarization calculations, *Geophys. J. R. astr. Soc.*, **87,** 917–948.

Zhdanov, M.S., Varentsov, I.M., Weaver, J.T., Golubev, N.G. & Krylov, V.A., 1997. Methods for modelling electromagnetic fields: results from COMMEMI - the international project on the comparison of modelling methods for electromagnetic induction, *J. Appl. Geophys.*, **37,** 133–271.

APPENDIX A

To explain the ill-conditioning related to spurious curl-free E-fields, let us analyse eigenvalues of the system matrix A. A good approximation of those eigenvalues are eigenvalues of the operator

$$\mathcal{L}(M) = \nabla \times \left(\frac{1}{\mu}\nabla \times M\right) + \mathrm{i}\omega\hat{\sigma} M. \tag{A1}$$

$\mathcal{L}$ should be defined on some suitable finite dimensional space, dependent on the mesh size h. First, let us consider infinite dimensional space of vector fields $M \in \mathcal{H}_0(\nabla\times, \Omega)$, with the additional assumption that $\nabla \times \frac{1}{\mu}\nabla \times M$ exists and is square integrable. Let the domain be a cube $\Omega = [0, M]^3$ with $\hat{\sigma}, \mu = \text{const}$. It is straightforward to verify that the eigenvectors of $\mathcal{L}$ are of the form

$$v = \begin{bmatrix} C_x \cos\left(\pi\frac{k_x}{M}x\right)\sin\left(\pi\frac{k_y}{M}y\right)\sin\left(\pi\frac{k_z}{M}z\right) \\ C_y \sin\left(\pi\frac{k_x}{M}x\right)\cos\left(\pi\frac{k_y}{M}y\right)\sin\left(\pi\frac{k_z}{M}z\right) \\ C_z \sin\left(\pi\frac{k_x}{M}x\right)\sin\left(\pi\frac{k_y}{M}y\right)\cos\left(\pi\frac{k_z}{M}z\right) \end{bmatrix} \tag{A2}$$

for $k_x, k_y, k_z \in \mathbb{N}$ where

$$C = \begin{bmatrix} C_x \\ C_y \\ C_z \end{bmatrix} = \begin{bmatrix} k_x \\ k_y \\ k_z \end{bmatrix}, \begin{bmatrix} -k_z \\ 0 \\ k_x \end{bmatrix} \text{ or } \begin{bmatrix} 0 \\ k_z \\ -k_y \end{bmatrix}. \tag{A3}$$

Defining $|k|^2 = k_x^2 + k_y^2 + k_z^2$ one can write the corresponding eigenvalues as:

$$\lambda = \mathrm{i}\omega\hat{\sigma}, \quad \frac{\pi^2|k|^2}{\mu M^2} + \mathrm{i}\omega\hat{\sigma}, \quad \frac{\pi^2|k|^2}{\mu M^2} + \mathrm{i}\omega\hat{\sigma}. \tag{A4}$$

By checking that $\mathcal{L}(v) = \lambda v$, one can verify that v and λ are the eigenvectors and eigenvalues of $\mathcal{L}$. For an infinite dimensional space, we have $3 < |k|^2 < \infty$, yet for a discretization, with spatial mesh parameter h, it would be:

$$3 \le |k|^2 \le O\left(3\left(\frac{M}{h}\right)^2\right). \tag{A5}$$

The upper bound above would be correct if we used a finite difference discretization of the Laplacian (Trottenberg *et al.* 2000). We use it for the curl as it is also a second-order differential operator. One could consider also that in a discretized version of $\mathcal{L}$, roughly speaking, the natural numbers k_x, k_y, k_z would be allowed to vary from 1 to M/h.

Let us look at those eigenvalues for some practical setting for magnetotellurics. Let $M = 10$ km, $\frac{M}{h} = 50$. The quantity $\frac{\pi^2|k|^2}{\mu M^2}$ is in the interval $[2 \times 10^{-1}, 6 \times 10^{+2}]$. The values of the first eigenvalue $i\omega\hat{\sigma}$ for conductivity corresponding to the Earth's subsurface ($\hat{\sigma} = 0.01\ \mathrm{Sm}^{-1}$) and air ($\hat{\sigma} = i\omega\epsilon_0$) are presented in Table A1. The corresponding condition numbers of the system matrix, defined as $\mathrm{cond}(A) = \frac{\max(|\lambda|)}{\min(|\lambda|)}$ are presented in Table A2. One can see that if a conductivity corresponding to the ground is used, the condition number increases as the frequency decreases, yet remains at a reasonable level of 10^{+5} even for frequency as small as 0.01 Hz. If conductivity of the air is used, the situation is different. As the frequency decreases, the condition number increases quadratically and reaches very large value of 10^{+16} for the frequency 0.01 Hz.

Table A1. Values of $|\omega\hat{\sigma}|$ for different σ and ω. Unit of $|\omega\hat{\sigma}|$ is S Hz m^{-1}.

ω	2π 100 Hz	2π 1 Hz	2π 0.01 Hz
Earth: $\hat{\sigma} = 0.01$ S m^{-1}	6.3	6.3×10^{-2}	6.3×10^{-4}
Air: $\hat{\sigma} = \mathrm{i}\omega\epsilon_0$	3.5×10^{-6}	3.5×10^{-10}	3.5×10^{-14}

Table A2. Condition number of the system matrix A as a function of frequency ω and $\hat{\sigma}$.

ω	2π 100 Hz	2π 1 Hz	2π 0.01 Hz
Earth: $\hat{\sigma} = 0.01$ S m^{-1}	$9.3 \times 10^{+1}$	$9.3 \times 10^{+3}$	$9.3 \times 10^{+5}$
Air: $\hat{\sigma} = \mathrm{i}\omega^2\epsilon_0$	$1.7 \times 10^{+8}$	$1.7 \times 10^{+12}$	$1.7 \times 10^{+16}$

In MTs, the domain contains both earth and air. Because of the presence of the air, the matrix is ill-conditioned. Nevertheless, the calculated electric field, approximated by solving eq. (8) using a direct solver, and using eq. (7) has improper values only in the air. The electric field below the Earth's surface does not suffer from numerical instability. It is also worth mentioning, that the magnetic field, calculated using the curl of electric field as in eq. (11) has proper values in all of the domain. It shows, that the error added to the electric field in the air is curl-free.

The condition number of the matrix gets this large because of the smallness of the eigenvalue $\lambda = \mathrm{i}\omega\hat{\sigma}$, corresponding to the first C in eq. (A3). Note that the corresponding eigenvector is curl-free, whereas the other two are not. Moreover the first eigenvector is equal to $\nabla\varphi$, where

$$\varphi = \frac{M}{\pi}\sin\left(\pi\frac{k_x}{M}x\right)\sin\left(\pi\frac{k_y}{M}y\right)\sin\left(\pi\frac{k_z}{M}z\right) \tag{A6}$$

and $\varphi|_{\partial\Omega} = 0$. This is not a coincidence. In fact, in this case the conductivity $\hat{\sigma}$ is constant in the domain, and the Hodge decomposition discussed in 'Divergence correction' section is the standard Helmholtz decomposition. The eigenvectors of $\mathcal{L}$ span the space $H_0(\nabla\times, \Omega)$ respecting the decomposition. The eigenvectors with the first C of eq. (A3) span the space $R(\nabla)$, the eigenvectors with the second and the third C of eq. (A3) span $R(\nabla)^{\perp_{\hat{\sigma}}}$. The eigenvectors form an orthogonal basis of $\mathcal{H}_0(\nabla\times, \Omega)$ and the spaces $R(\nabla)$ and $R(\nabla)^{\perp_{\hat{\sigma}}}$ are orthogonal.

APPENDIX B

Here we present a 3-D high frequency test similar to the one of Fig. 11 for the 2-D hill. Again, if skin depth in the subsurface is much less than the scale of topographic variation, the incident EM wave should refract normal to the slope and behave as if the surface is locally flat and horizontal (Wannamaker *et al.* 1986). For each receiver considered in the Mount Erebus model, we rotate the coordinate system such that X and Y axes are parallel to the slope and Z axis is perpendicular to the slope. The MT response is calculated in those coordinates. The apparent resistivity and impedance phase calculated using Z_{xy}, $-Z_{yx}$, and $\frac{1}{2}(Z_{xy} - Z_{yx})$ as a function of frequency

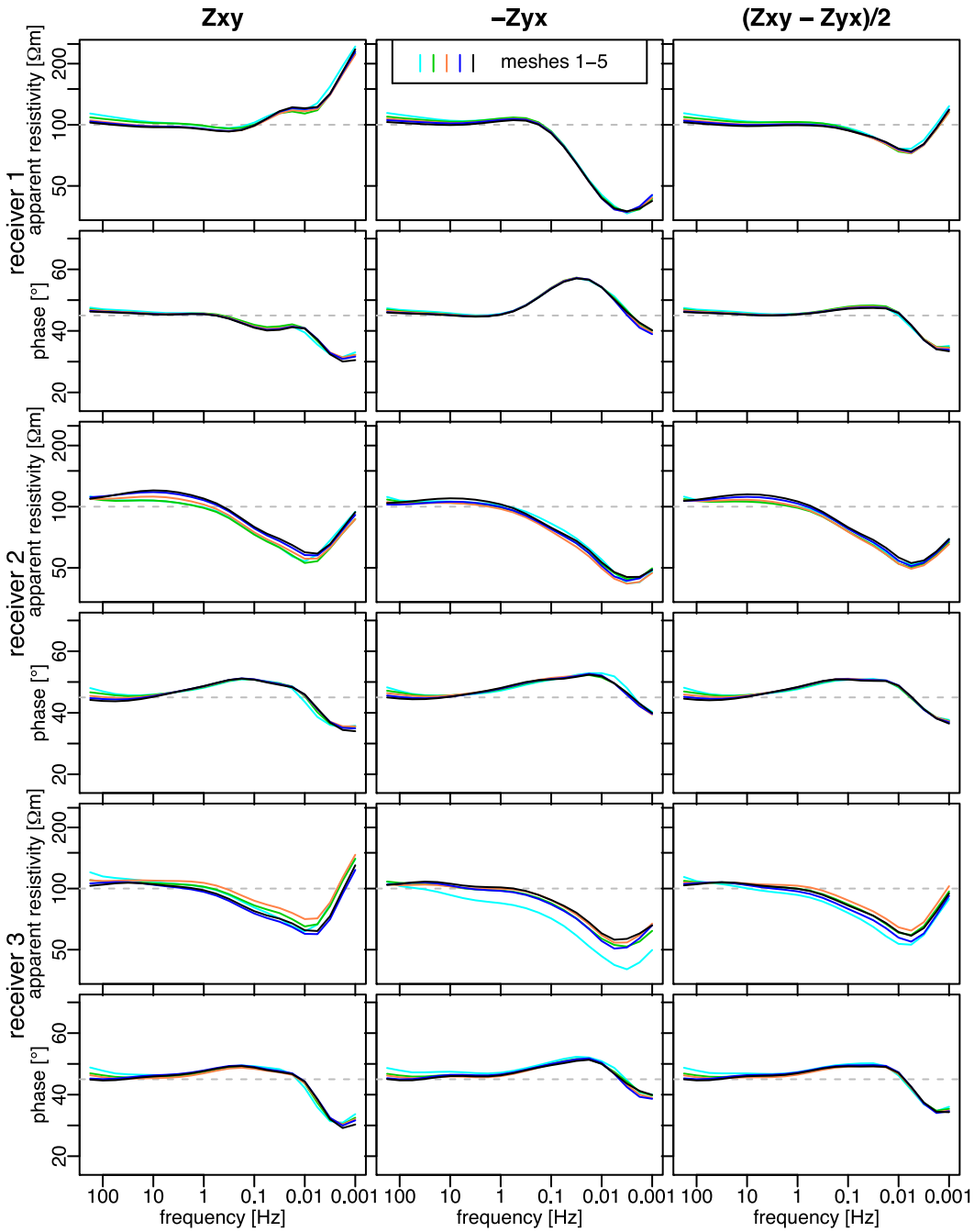

Figure B1. Apparent resistivity and impedance phase as a function of frequency for three receivers of the Mount Erebus model. The coordinate system in which the impedance is calculated has *X* and *Y* axes parallel to the slope and the *Z* axis perpendicular to it.

are presented in Fig. B1. We observe that as frequency becomes high, towards 100 Hz, the apparent resistivity approaches 100 Ωm and impedance phase approaches 45°, which is the response of the 100 Ωm half-space. Similarly, the tipper elements (see Fig. B2) approach 0 at high frequencies. The best results are obtained for meshes 4 and 5 where cell thicknesses become a smaller fraction of skin depth. The elements next to the Earth's surface have thickness of 100 m for mesh 1 and 25 m for mesh 5. Results begin to degrade much above 100 Hz even for mesh 5, and would require even finer discretization.

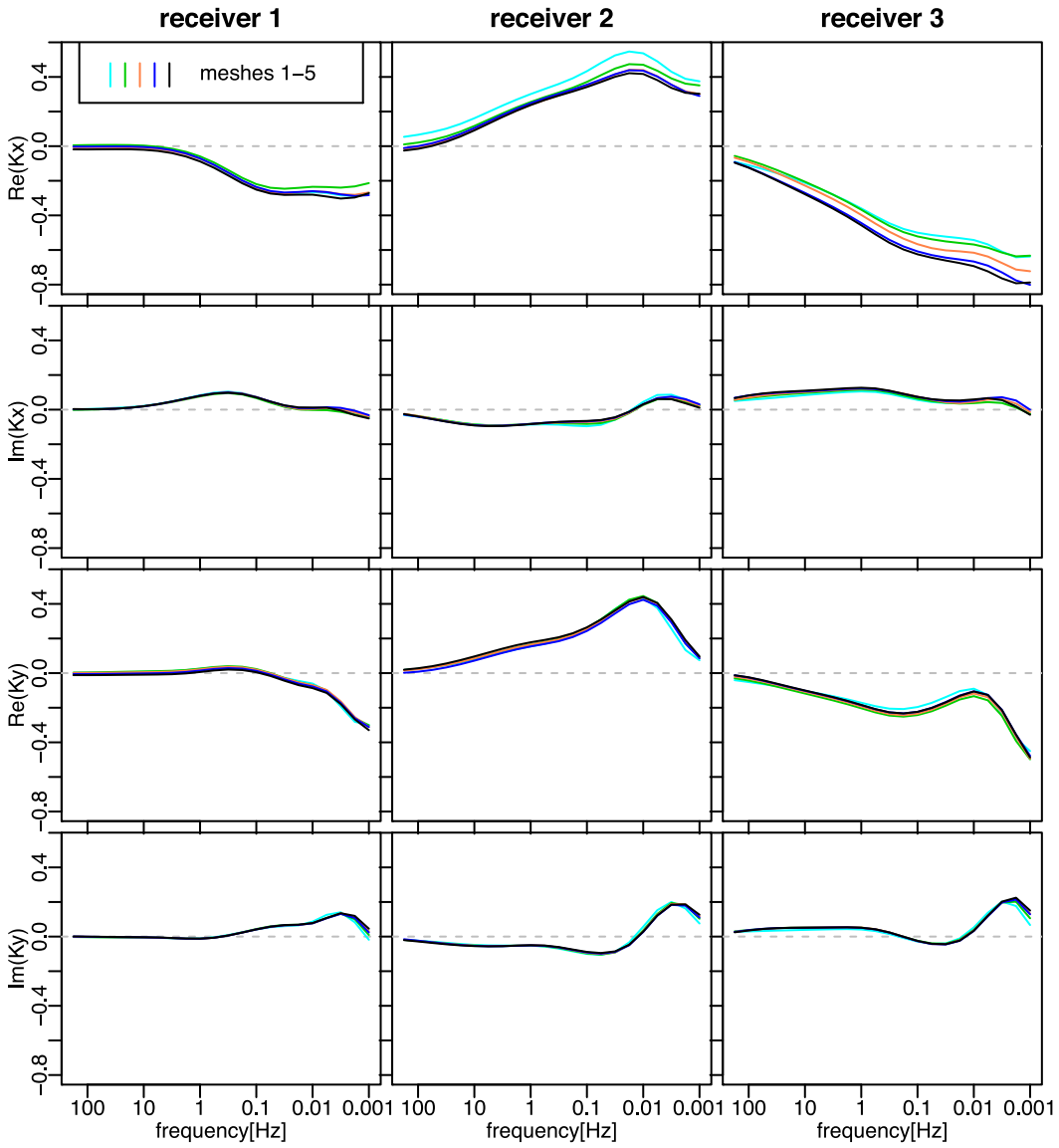

Figure B2. Complex tipper elements as a function of frequency for three receivers of the Mount Erebus model. The coordinate system in which the tipper is calculated has *X* and *Y* axes parallel to the slope and the *Z* axis perpendicular to it.